NUMERICAL SIMULATION OF PROPPANT TRANSPORT IN FIELD-SCALE FRACTURES WITH THE MULTI-PHASE PARTICLE-IN-CELL METHOD

A Thesis

by

ZHUO ZHANG

Submitted to the Office of Graduate and Professional Studies of
Texas A&M University
in partial fulfillment of the requirements for the degree of

MASTER OF SCIENCE

Chair of Committee,	Kan Wu
Committee Members,	Nobuo Morita
	Keshawa Shukla
Head of Department,	Timothy Jacobs

May 2020

Major Subject: Interdisciplinary Engineering

ABSTRACT

Slickwater fracturing is one of the key techniques for successful development of unconventional reservoirs. However, due to the low viscosity of slickwater, proppant-suspending capacity is very limited. Proppants settle down quickly in the fracture and form a proppant bed. The traditional continuous model for simulating proppant transport cannot capture the main physics of proppant transport in the slickwater and predict proppant placement. The models of Computational Fluid Dynamics Discrete Element Method (CFD-DEM) are computationally demanding and only can simulate proppant transport in the small-scale fractures. This study applied the Multiphase Particle-in-Cell (MP-PIC) model to simulate the proppant transport process in a field-scale fracture.

The present simulation attempts to study the effect of crucial factors (fracture height, proppant concentration, fluid viscosity, and injection rate) on proppant placement. We constructed a 180 m long vertical fracture for simulation. When we injected 40/70 mesh proppants into this field scale fracture, the case studies can be performed. Our simulation results show as follows:

- When the fracture reaches a certain height, increasing fracture height has an insignificant effect on proppant placement. Decreasing this certain height can result in longer proppant length due to a stronger wash-out effect.
- The viscosity is sensitive to the proppant height. The proppant bed height will decrease significantly with a larger fluid viscosity.
- The injected slurry with relatively low proppant concentration can form a longer proppant length.

- Changing the injection rate without adding more proppant will not influence the final proppant distribution.
- Proppants injected at different times can distribute differently with various injection rate.
- The higher injection rate and proppant concentration can respectively help injected proppants reach proppant dune height and maximum fracture length faster.

ACKNOWLEDGEMENTS

I would like to thank my committee chair, Dr. Wu, and my committee members, Dr. Morita, Dr.Shukla, for their guidance and support throughout the course of this research.

Thanks also go to my friends and colleagues and the department faculty and staff for making my time at Texas A&M University a great experience.

CONTRIBUTORS AND FUNDING SOURCES

This work was supervised by a thesis committee consisting of Dr. Kan Wu [advisor] and Dr. Nobuo Morita of the Department of [Petroleum Engineering] and Dr. Keshawa Shukla of the Department of [Interdisciplinary Engineering].

The model code was provided and calibrated by Shaowen Mao of Department of [Petroleum Engineering].

All other work conducted for the thesis was completed by the student independently.

No funding was provided for the graduate study.

NONMENCLATURE

MP-PIC	Multiphase Particle-in-Cell
CFD	Computational Fluid Dynamics
DEM	Discrete Element Method
α_f	Fluid volume fraction
ρ_f	Fluid density, kg/m^3
t	Time, s
u_f	Fluid velocity, m/s
p	Fluid pressure, Pa
F_{fp}	Momentum change between fluid and particle, kg·m/s
g	Gravity acceleration, m/s^2
τ_f	Fluid microscopic viscous stress, Pa
S_{ij}	Nonhydrostatic stress tensor, Pa
τ_{ij}	Deviatoric stress, Pa
μ_f	Fluid viscosity, Pa·s
δ_{ij}	Isotropic second-order tensor, Pa
ϕ	Probability distribution
x	Particle position, m
u_p	Particle velocity, m/s
ρ_p	Particle density, kg/m^3
V_p	Particle Volume, m^3

$\left(\frac{\partial f}{\partial t}\right)_{coll}^{D}$	Collision damping term
A	Particle acceleration, m/s^2
τ_p	Resistance of particles, Pa
D_p	Drag force coefficient
C_d	Dimensionless coefficient of interphase drag force
Re	Reynolds number
r_p	Radius of particles, m
α_{cp}	Particle volume fraction under condition of close packing
L	Fracture length, m
W	Fracture width, m
H	Fracture height, m
C	Proppant concentration, kg/m^3
D	Proppant diameter, m
V	Inlet slurry velocity, m/s

TABLE OF CONTENTS

Page

LIST OF FIGURES

Page

LIST OF TABLES

Page

1. INTRODUCTION*

1.1 Hydraulic Fracturing

Hydraulic fracturing has become the main solution for hydrocarbon recovery in unconventional reservoirs. During the process, the fluid is pumped into the reservoir at sufficiently high pressure, and the reservoir rock will crack. Keep pumping of the fluid at this high pressure will propagate the fracture into the subsurface reservoir. A slurry can be pumped into the fracture to generate a slab-shaped zone of high permeability known as a hydraulic fracture. The created fracture geometry is closely related to the well productivity (Chu et al., 2019a; Chu et al., 2019b； Zhang et al., 2018; Zhang et al., 2020; Li et al., 2019; Li et al., 2020; Guo et al., 2019). The main controlling factor of the conductivity and closure behaviors of induced fractures is the distribution of injected proppant (Liu et al., 2017; Liu et al., 2018). Therefore, understanding the proppant transport behavior plays an important role in increasing well productivity.

1.2 Proppant Transport in Slickwater Fracturing

Slickwater fracturing has commonly been used in unconventional resources. It not only reduces the environmental impact and cost but also generates the complexity of created fracture networks (Tang et al., 2019; Weng, 2015; Wu et al., 2018; Rui et al., 2017). However, proppant transport behaviors are complex in slick water. This is because the proppant carried by low viscous fluid will settle early instead of suspension, leading to the unpropped area and reduced fracture

* Reprinted with permission from "Numerical Study of Proppant Transport in Field-scale Fractures for Slickwater Fracturing" by Zhang, Z., Mao, S., Shang, Z., Chun, T and Wu, K. 2020. Proceedings of the 54th US Rock Mechanics/Geomechanics Symposium, Copyright [2020] by American Rock Mechanics Association. paper ARMA 20-1170

conductivity (Donaldson et al., 2014). As a result, numerous studies of numerical simulations and experimental observations of proppant transport were conducted.

1.3 Literature Review

1.3.1 Proppant Transport Experiments

Kern et al. (1959) conducted the first experiment to explore proppant transport. Schols and Visser (1974) then introduced the three consecutive phases of proppant bank buildup and confirmed those phases by experiment. Blot and Medlin (1985) developed a theory of three types of sand transport behaviors using an analytical model and verified the theory by experiment (Medlin et al., 1985). The three sand transport behaviors are viscous drag, turbulence and bed load transport. Babcock et al. (1967) found that factors including proppant diameters and density, pumping rate, and fluid viscosity can influence proppant distribution differently in laminar flow and turbulence flow. The proppant dune shape in constant fracture geometry can also be predicted based on those factors. Clark and Guler (1983) reported that the proppant settling velocity is related to fluid and proppant parameters. The large-scale model was firstly introduced by Sievert et al. (1981) to investigate the effects of proppant concentration and fluid viscosity in both Newtonian and non-Newtonian fluid. Shah and Lord (1990) proposed that the critical deposition and resuspension velocity of fracturing fluid can slightly increase in low viscous fluid with an increasing proppant concentration. McMechan and Shah (1991) used a field-scale experiment to study the impact of concentration on proppant settling in different fracturing fluids. Barree and Conway (1994) used commercial software and found the injection rate and proppant ramping can modify the proppant placement. Clark and Zhu (1995) demonstrated the

effect of increasing viscosity and its different effects of Newtonian and non-Newtonian fluids. Later on, the effect of fracture width on proppant placement was studied in the experiment of Liu and Sharma (2005). Sahai et al. (2014) examined and explained this effect from primary to secondary fracture slots in complex fracture networks experiment. Alotaibi and Miskimins (2015) extended this work and developed an analytical model to predict the proppant bed height in the primary fracture for 30/70 mesh sand. The same lab model was used by Ahmad and Miskimins (2019) to study the effect of proppant type. Analysis of factors controlling proppant transport became popular in experiments of recent years. Mohammed Ba Geri and Abdulmohsin Imqam (2019) investigated the impact of perforation technique, shear rate and proppant size on proppant distribution. Four dominant mechanisms of proppant transport were noticed during the experiment. Tong and Mohanty (2016); Chun et al. (2019a) both tested the effect of proppant size and injection rate in a T-shaped fracture. The effect of inclination angle and proppant size in an inclined fracture were investigated by Mohammed Ba Geri (2018); Chun et al. (2019b). Although recent experimental works have been carried out to study proppant transport behaviors in complex fractures, no existing experiment study focused on the proppant transport in field-scale vertical fracture. Moreover, scaling up observations from small laboratory scale to field scale can cause unavoidable uncertainties. Therefore, numerical models were developed to provide complementary insights to learnings from experimental work.

1.3.2 Proppant Transport Numerical Simulations

Two main approaches, as the basis of numerical models, are accessible to simulate the mechanism of two-phase flow: Eulerian-Eulerian method and Eulerian-Lagrangian method. The

Eulerian-Eulerian model considers both the fluid and particle as interpenetrating continua and solves both momentum conservation equation separately (Ariyaratne et al., 2018). Kong et al. (2016) once validated this model by showing consistency with the experimental observation by Clark (2006). By employing this model, Kong and McAndrew (2017) indicate fracture width and viscosity can significantly impact on proppant placement, and the dune height will rise with an increasing injection rate. This model is reported to be applied by major large-scale proppant transport processes in previous work because it takes less computational cost (Zeng et al., 2019)). Since this approach has limitations in capturing variations of particle properties, the Eulerian-Lagrangian method has been used. This approach treats particles by tracking a large number of particles using a Newtonian equation. As an example, the Computational Fluid Dynamics Discrete Element Method (CFD-DEM) is commonly used in recent work for its high accuracy (Zhang et al., 2019). Kou et al. (2018a) validated CFD-DEM and extend this work to solve large scale problems (Kou et al., 2018b). However, the computational cost is too high to address the real field problems so that the CFD-DEM is unable to simulate the physical behaviors of proppant transport in the field-scale.

1.4 Problem Summary

From previous experimental observations and numerical simulations of proppant transport, we summarize the distinct behaviors of proppant delivering in hydraulic fracturing:

- The proppant placement differs with key factors, such as proppant diameter, density and concentration, pumping rate, fluid viscosity, and fracture geometry (Babcock et al., 1967; Mao et al., 2019; Zeng et al., 2019; Hu et al., 2018; Chun et al., 2019).

- The relatively small grades of proppant (40/70 and 100 mesh) carried by a low viscosity fluid with friction reducer to allow high pump rate is the preferred fracturing treatment in an unconventional gas play (Patel et al., 2014; Ba Geri et al., 2019).
- Viscosity has a complex impact on proppant placement. When fluid viscosity is between 0.1cp to 10 cp (Zeng et al., 2019), the proppant bed height will decrease with higher viscosity fluid. While fluid viscosity increases from 10 cp to 100 cp, higher viscosity leads to a higher proppant bed in fracture (Kong and McAndrew, 2017).
- The proppant bed height can first increase and then decrease with the increase of proppant concentration (Hu et al., 2018).
- With an increasing injection rate, the proppant length will increase while the proppant equilibrium height decreases. Besides, the proppant will evenly distribute (Hu et al., 2018).
- The higher fracture height can suspend more proppant and transport proppant further in a small-scale simulation (Suri et al., 2019). The effect of fracture height is negligible for very high fracture in large scale simulation, and the decrease of fracture height can increase proppant bed wash-out and increase proppant transport distance (Hu et al., 2018).

Although propositions from previous works can give us intuitive insights into the mechanism of proppant settling, we found that fractures that used in the majority of numerical and experimental works are in a small scale (within 10 m) rather than a field-scale (larger than 100 m). Despite some recent numerical works performed validation by reaching the consistency

with existing lab work, scaling up observations to a field scale is problematic when focusing fracture geometry.

In our previous paper (Zhang et al., 2020), the three-dimensional MP-PIC method was applied to explore the factors controlling proppant transport in field-scale fractures. The MP-PIC method was verified to be a powerful tool for proppant transport simulation that can take massive computational cost. Moreover, with the analysis of proppant distribution in the age plot, the detailed mechanism which can help us address complicated engineering problems was captured.

1.5 Objectives

In this thesis, the same input parameter was applied at this time, and one more case concerning the effect of fracture height was added to the original 14 cases. We would draw additional age plots and one particle settling plot to figure out the mechanism behind the effects of fracture height, fluid viscosity, proppant concentration and injection rate. The results of this thesis would better explain the effects of each factor.

2. METHODOLOGY*

2.1 Introduction of Multiphase Particle-in-Cell Method (MP-PIC)

The MP-PIC method termed in the Eulerian-Lagrangian method was introduced by (Andrews and O'Rourke, 1996) as an extension of the PIC methods by separating gas and particle velocities. For the particle phase, this method applies a Liouville equation for the distribution function of particles, including particle positions, velocities, and sizes. While it solves the fluid as the continuous phase by the mass and momentum equations, which was a typical Eulerian continuum description (Ariyaratne et al., 2018). This coupled feature can help produce a formulation that can readily handle particle characteristics. Moreover, this model divides the distribution of particles into finite computational parcels according to their similarity of mass density, volume, velocity, and location. This characteristic allows this method to significantly reduce computational requirements with a small impact on its accuracy. For these reasons, this model is suitable for addressing proppant transport in the field scale.

2.2 Governing Equations for MP-PIC

The methodology in the thesis attempted to replicate Zhang et al. (2020)'s governing equations that followed Mao et al. (2019)'s and Mao et al. (2020)'s work since the same model code was applied.

* Reprinted with permission from "Numerical Study of Proppant Transport in Field-scale Fractures for Slickwater Fracturing" by Zhang, Z., Mao, S., Shang, Z., Chun, T and Wu, K. 2020. Proceedings of the 54th US Rock Mechanics/Geomechanics Symposium, Copyright [2020] by American Rock Mechanics Association. paper ARMA 20-1170

2.2.1 Governing Equations for Fluid Phase

The fluid motion is governed by 3D equations in the Eulerian framework shown as follows:

$$\frac{\partial(\alpha_f \rho_f)}{\partial t} + \nabla \cdot \left(\alpha_f \rho_f u_f\right) = 0 \quad , \tag{1}$$

where the α_f is the fluid volume fraction, ρ_f is the fluid density (in kg/m^3), t is the time (in s) and u_f is the fluid velocity (in m/s).

The momentum equation is given by a modification of the Navier-Stokes equations,

$$\frac{\partial(\alpha_f \rho_f u_f)}{\partial t} + \nabla \cdot \left(\alpha_f \rho_f u_f u_f\right) = -\nabla p - F_{fp} + \alpha_f \rho_f g + \nabla \cdot \alpha_f \tau_f \quad , \tag{2}$$

where p is the fluid pressure (in Pa), F_{fp} is the momentum change between fluid and particle (in kg·m/s), g is the gravity acceleration (in m/s^2) and τ_f is fluid microscopic viscous stress (in Pa).

The nonhydrostatic stress tensor S_{ij} is solved by the following equation,

$$S_{ij} = \frac{1}{2}\left(\frac{\partial u_i}{\partial x_j} + \frac{\partial u_j}{\partial x_i}\right) \quad , \tag{3}$$

where $\frac{\partial u_i}{\partial x_j}$ and $\frac{\partial u_j}{\partial x_i}$ are both the deformation tensor (in Pa).

The equation for determining the stress of Newtonian fluid is shown below,

$$\tau_{ij} = 2\mu_f S_{ij} - \frac{2}{3}\mu_f \delta_{ij} \frac{\partial u_i}{\partial x_j} \quad , \tag{4}$$

where τ_{ij} is the deviatoric stress (in Pa), μ_f is the fluid viscosity (in Pa·s) and δ_{ij} is the isotropic second-order tensor (in Pa).

2.2.2 Kinetic Equations for Particle Phase

The particle phase is governed by the probability distribution function, $\phi(x, u_p, \rho_p, V_p, t)$, which describes the dynamic behavior of particles,

$$\frac{\partial \phi}{\partial t} + \nabla \cdot (\phi u_p) + \nabla_{u_p} \cdot (\phi A) = \left(\frac{\partial f}{\partial t}\right)_{coll}^{D} \quad , \tag{5}$$

where ϕ is the probability distribution proposed in (Andrews and O'Rourke, 1996), x is the particle position (in m), u_p is particle velocity (in m/s), ρ_p is particle density (in kg/m^3) and V_p is the particle volume (in m^3). $\left(\frac{\partial f}{\partial t}\right)_{coll}^{D}$ is the collision damping term, A is particle acceleration (in m/s^2) respectively impacted by an interphase drag force, dynamic pressure gradient, dynamic pressure gradient, gravity and interparticle stress gradient,

$$A = \frac{du_p}{dt} = D_p(u_f - u_p) - \frac{1}{\rho_p}\nabla p + g - \frac{1}{\alpha_p \rho_p}\nabla \tau_p \ , \tag{6}$$

where τ_p at the RHS of the following equation represents the resistance of particles (in Pa),

$$D_p = C_d \frac{3}{8}\frac{\rho_f}{\rho_p}\frac{|u_f - u_p|}{R_p} \quad , \tag{7}$$

where D_p is the drag force coefficient from the model developed by (Wen, 1966), and is shown as follows:

$$C_d = \begin{cases} \frac{24}{Re}\left(\alpha_f^{-2.65} + \frac{Re^{\frac{2}{3}}}{6}\alpha_f^{-1.78}\right), Re < 1000 \, , \\ 0.44\alpha_f^{-2.65}, Re > 1000 \end{cases} \tag{8}$$

$$Re = \frac{2\rho_f |u_f - u_p| r_p}{\mu_f} \ , \tag{9}$$

$$r_p = \left(\frac{3V_p}{4\pi}\right)^{\frac{1}{3}} \quad , \tag{10}$$

where C_d represents the dimensionless coefficient of interphase drag force. Re is the Reynolds number governed by Eq. (9). r_p is the radius of particles (in m) and V_p is the particle volume (in m^3).

In this thesis, an extension of the model of (Harris and Crighton, 1994) is applied for determining isotropic interparticle stress:

$$\tau_p = \frac{P_s \alpha_p^{\beta}}{max[\alpha_{cp} - \alpha_p, \varepsilon(1-\alpha_p)]} \ , \tag{11}$$

where P_s is a constant with units of pressure, β is a constant (Auzerais et al., 1988) recommend between 2 to 5, α_{cp} is the particle volume fraction under the condition of close packing, ε is a number on the order of 10^{-7}, this interparticle stress enables the volume fraction to reach possible close pack (Snider, 2001).

2.2.3 Interphase coupling

The rate of momentum exchange F_{fp} when the momentum of the fluid is coupling to the particle is defined from the particle population distribution as:

$$F_{fp} = \iiint \phi V_p \rho_p \left[D_p(u_f - u_p) - \frac{1}{\rho_p} \nabla p \right] dV_p d\rho_p du_p \ . \tag{12}$$

2.3 Model Validation

The validation process of this model is achieved by comparing our results with small scale indoor lab results of Tran et al. (2017) and the results of CFD-DEM (Kou et al., 2018a). This experiment examined proppant transport in a high viscosity fluid. In the experiment, 30/60 mesh size sand was injected in linear guar (3.5 cp) into a vertical slot for 210 seconds. **Figure 1** shows the small-scale experimental slot. The same proppant transport behavior of the experiment was captured in the simulation result of Kou et al. (2018a). We applied the same parameters in our model to compare both of their results. The input parameters collected from the experiment of Tran et al. (2017) were listed in **Table 1**.

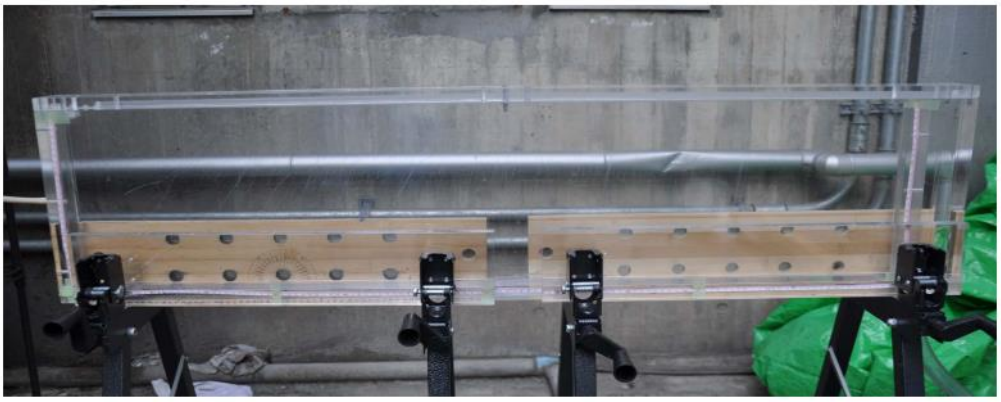

Figure 1. Proppant Transport Slot Equipment in Experiment of Tran et al. (2017)

Table 1. Simulation Parameters for Model Validation, Reprinted from Zhang (2020)

Parameter	Symbol	Unit	Value
Fracture length	L	m	1.2
Fracture width	W	m	0.005
Fracture height	H	m	0.3
Proppant concentration	C	kg/m^3	99
Proppant diameter	D	mm	0.25~0.6
Proppant density	ρ_p	kg/m^3	2650
Clean fluid density	ρ_f	kg/m^3	1000
Clean fluid viscosity	μ_f	Pa*s	3.5×10^{-3}
Inlet slurry velocity	V	m/s	0.014

After we completed the simulation in the same scale fracture, consistent simulation results were obtained. **Figures 2-7** show the comparison between simulation and experiment result of proppant distribution after 30, 90, 180 s injection. As is shown in the figures, regardless of the small difference of proppant suspension, the MP-PIC method captured the complex physics of particles. Besides, compared to the experiment results shown in half of the experimental slot, our simulation results obtained the same size proppant beds for every time step.

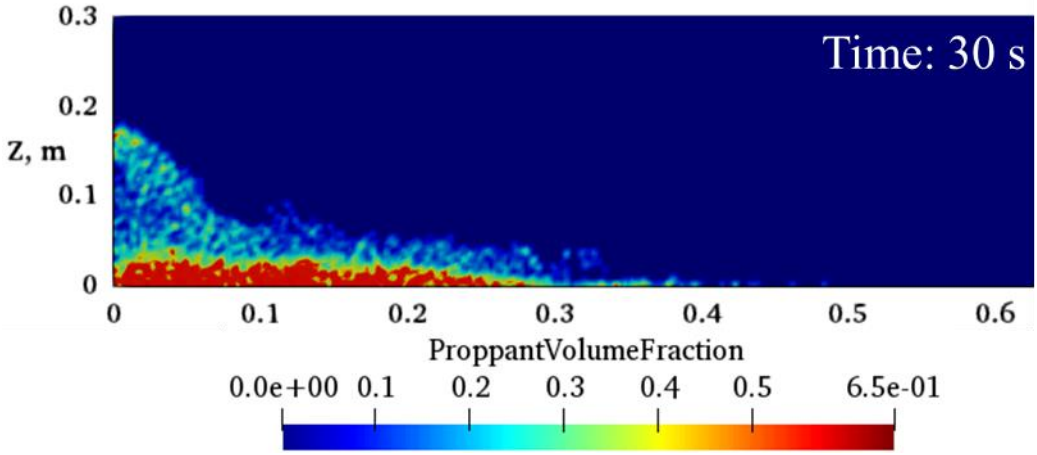

Figure 2. Proppant Volume Fraction using MP-PIC Method with 30 s Injection

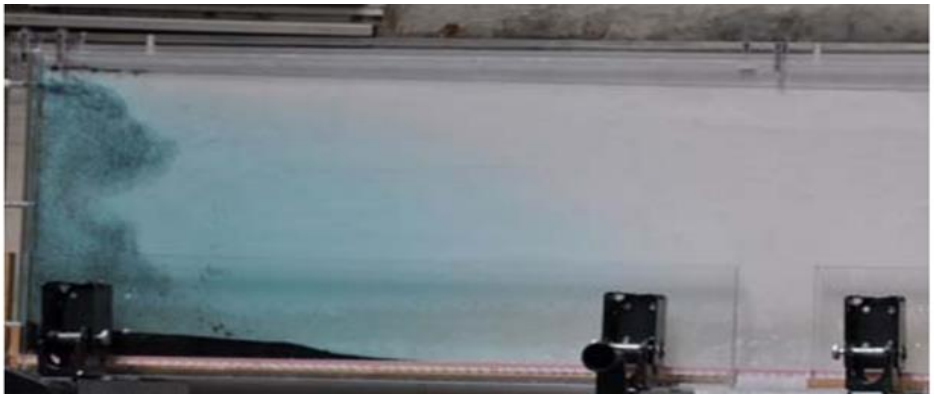

Figure 3. Experiment Observation of Tran et al. (2017) with 30 s Injection

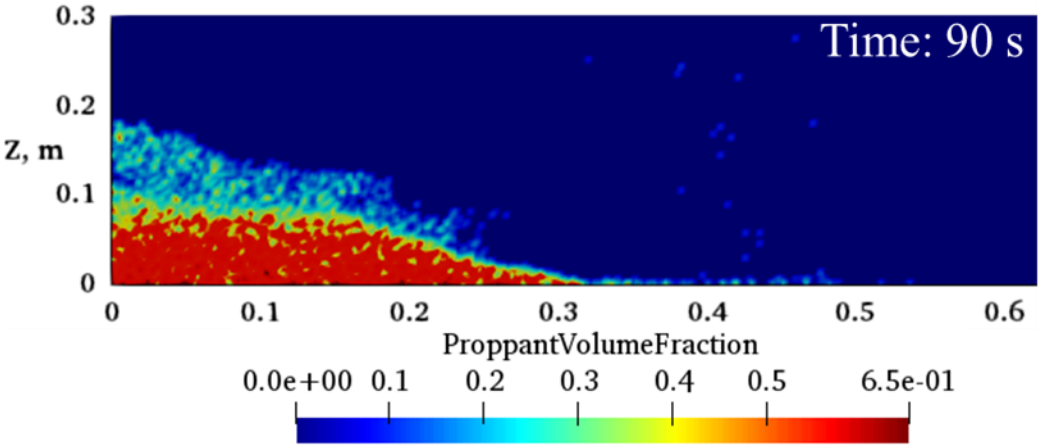

Figure 4. Proppant Volume Fraction using MP-PIC Method with 90 s Injection

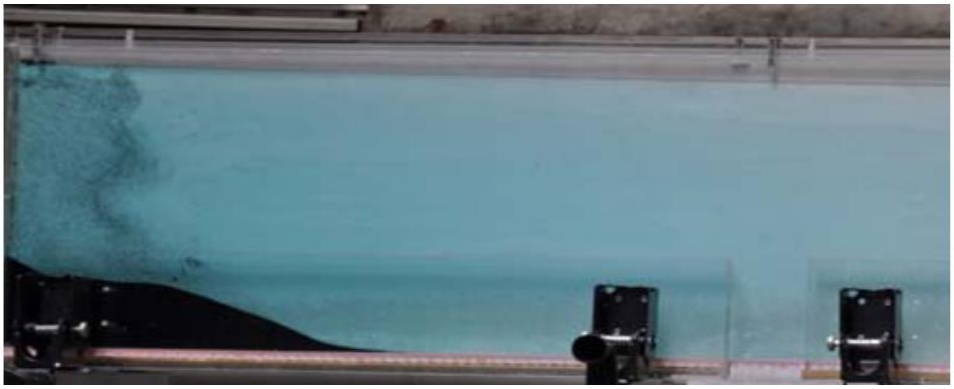

Figure 5. Experiment Observation of Tran et al. (2017) with 90 s Injection

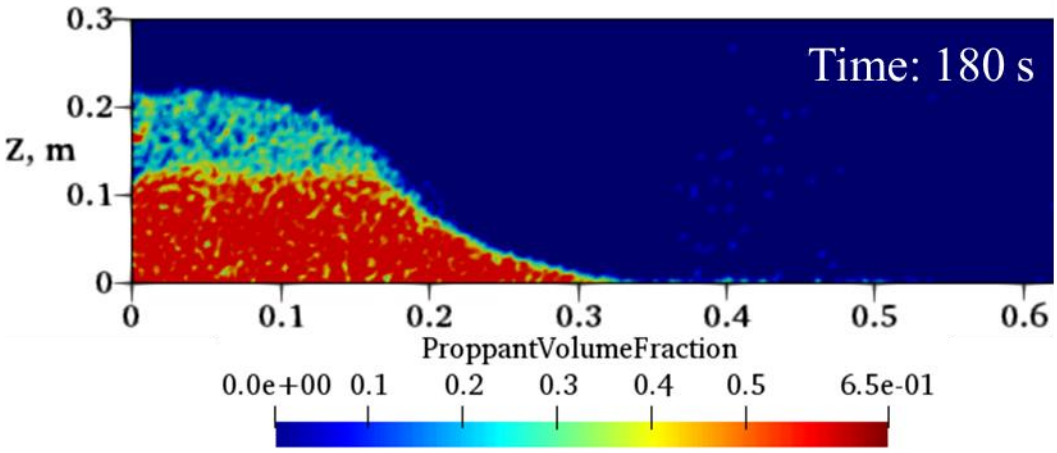

Figure 6. Proppant Volume Fraction using MP-PIC Method with 180 s Injection

Figure 7. Experiment Observation of Tran et al. (2017) with 180 s Injection

Figure 9 shows the experiment observation at 210 s, the equilibrium dune height was at half of the experimental slot height, and fewer proppants were suspended on the top of the dune. Proppant length was at one-quarter of the slot length. **Figure 8** shows the consistent proppant distribution in our simulation results, proppants with low volume fraction were suspended at the same position, the proppant length and height are almost the same as that in the experiment. After that, we plot the particle settling velocity to compare results in CFD-DEM. As shown in **Figure 11**, the proppants with relatively high velocity (shown in red color) entered the fracture, moved along the top of the dune, and gradually lose momentum. Finally, they settled at nearly zero velocity (shown in dark blue color) (Kou et al., 2018a). **Figure 10** reveals the same trend of particle settling velocity from the simulation result of MP-PIC model.

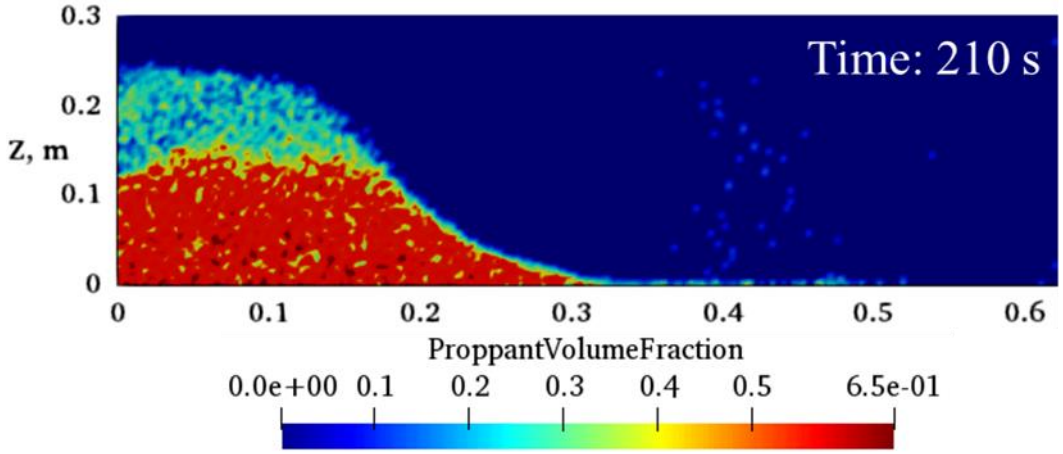

Figure 8. Proppant Volume Fraction using MP-PIC Method with 210 s Injection, Reprinted from Zhang (2020)

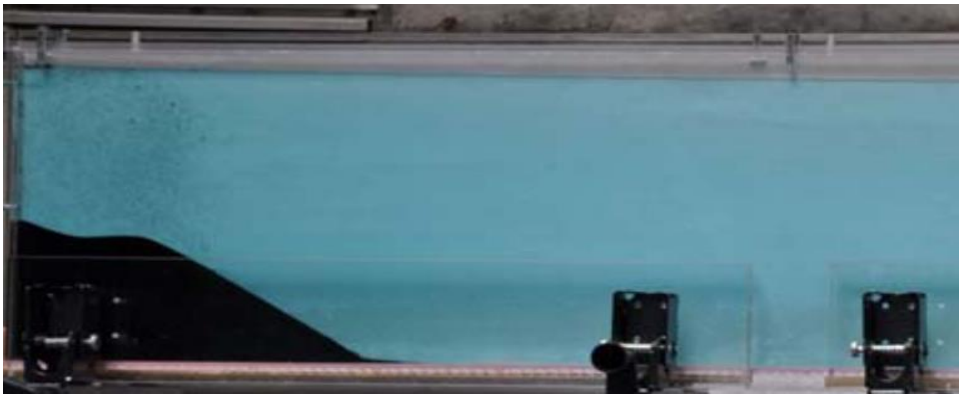

Figure 9. Experiment Observation of Tran et al. (2017) with 210 s Injection, Reprinted from Zhang (2020)

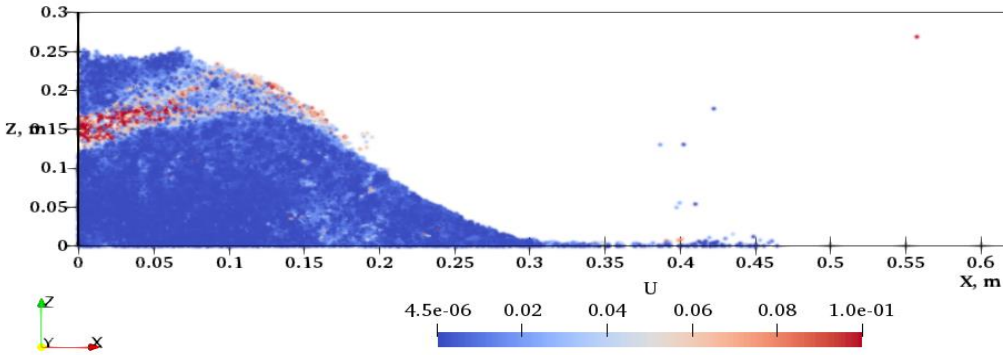

Figure 10. Particle Settling Velocity in Simulation Result Using the MP-PIC model, Reprinted from Zhang (2020)

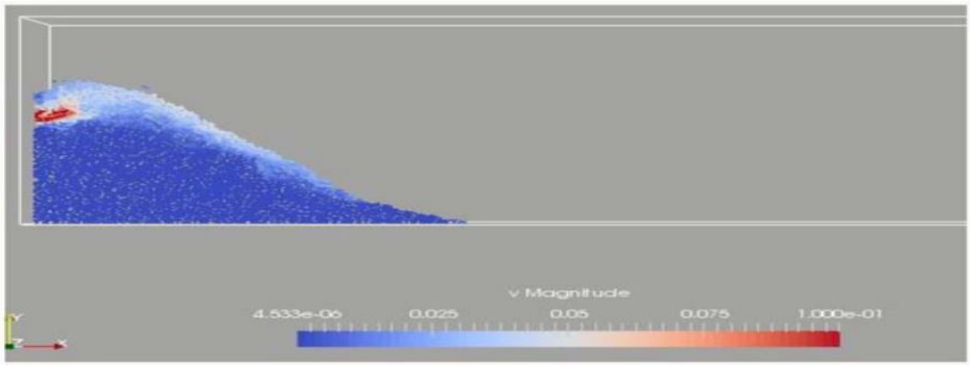

Figure 11. Particle Settling Velocity in Simulation Result of Kou et al. (2018), Reprinted from Zhang (2020)

Base on the comparison between the experiment results and CFD-DEM simulation results, we found that the MP-PIC method can provide accurate simulation results of proppant placement. Other than that, it can capture the crucial physical features of the particle-fluid system. Therefore, our proposition based on the simulation result of this model can be convincing.

3. RESULT AND DISCUSSION*

3.1 Case Setup

A field-scale vertical rectangular slot is constructed as a half wing of a fracture for our simulation. The length and width of this slot are respectively 180 m (590 ft) and 7.62 mm (0.3 in). A 3 m (118 in) long and the same wide rectangular injection area was designed. Although the injection length is defined to be larger than the actual wellbore size, since the injection flow has a very high velocity and varied from 9.5 to 38 m/s, the simulation would not get affected by this modification (Tsai et al., 2012). The computational cell configuration of this vertical fracture slot is shown in **Figure 12**. The flow starts from the center of the left side and exits through the right side of the slot. Additionally, a nonuniform size of 40/70 mesh sand is used. The slot size and sand are kept constant for all cases in the simulation. Magnitudes of fracture height, viscosity, proppant concentration, and injection rate for each case are listed in **Table 2**.

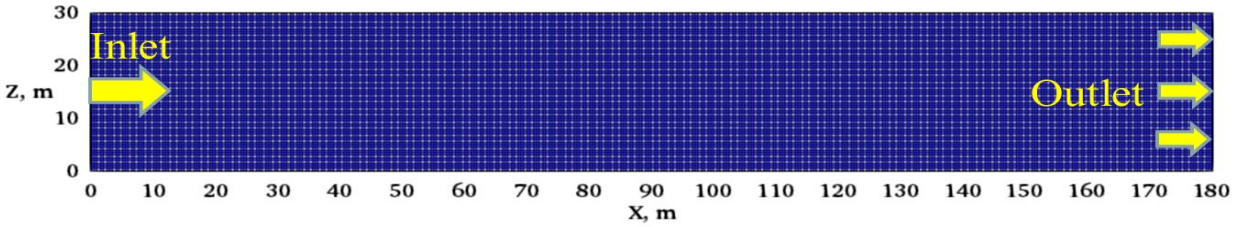

Figure 12. Computational Cell Configuration of A Vertical Fracture, Reprinted from Zhang (2020)

The fracture height of the base case (case 1) was established at 30 m. 2 lb/gal of 40/70 mesh sand was pumped at 15 bpm into the fracture for 30 mins. The fluid viscosity was 1 cp for

* Reprinted with permission from "Numerical Study of Proppant Transport in Field-scale Fractures for Slickwater Fracturing" by Zhang, Z., Mao, S., Shang, Z., Chun, T and Wu, K. 2020. Proceedings of the 54th US Rock Mechanics/Geomechanics Symposium, Copyright [2020] by American Rock Mechanics Association. paper ARMA 20-1170

slickwater. Since the effect of fracture height and fluid viscosity on proppant transport is complex, another 5 cases (cases 2-6) and 5 cases (cases 7-11) were respectively configured to study the impact of fracture height and fluid viscosity on proppant transport. After that, two sets of 2 cases (cases 12-13 and cases 14-15) were conducted accordingly to study the effect of proppant concentration and injection rate. For these 4 cases, injection time was normalized to keep injected proppant volume the same. All parameters of the total 15 cases can be found in **Table 2**.

Table 2. Simulation Parameters for Sensitivity Analysis, Reprinted from Zhang (2020)

No.	Fracture Height (m)	Viscosity (10^{-3} Pa*s)	Concentration (kg/m^3)	Injection Rate (m/s)	Time (mins)
1	30	1	240 (2 lb/gal)	1.74 (15 bpm)	30
2	15	1	240	1.74	30
3	25	1	240	1.74	30
4	45	1	240	1.74	30
5	75	1	240	1.74	30
6	90	1	240	1.74	30
7	30	0.5	240	1.74	30
8	30	2	240	1.74	30
9	30	3	240	1.74	30
10	30	10	240	1.74	30
11	30	30	240	1.74	30
12	30	1	180 (1.5 lb/gal)	1.74	24
13	30	1	300 (2.5 lb/gal)	1.74	40
14	30	1	240	1.16	45

				(10 bpm)	
15	30	1	240	2.32 (20 bpm)	22.5

3.2 Case Study 1 – Base Case

Figures 13-15 show the simulation results of the base case. Three stages different from phases of (Schols and Visser, 1974) were presented in our simulation of proppant transport with slick water in a field-scale fracture. In the early stage, most proppants quickly settled and formed a uniform proppant bed near the injection point. Fewer proppants were suspended on the top. In the mid stage, without reaching the equilibrium height near the injection point, the proppant bed greatly grew in both length and height. More proppants placed far from the injection point. For the late stage, when the proppant bed at the middle of fracture reached the equilibrium proppant height, some proppants went further and accumulated to create the proppant dune eventually.

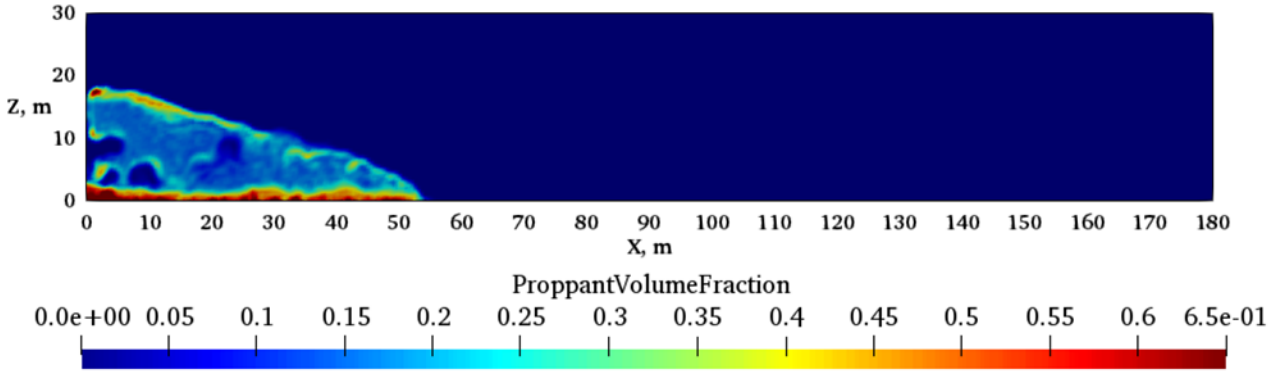

Figure 13. Proppant Transport in the Early Stage

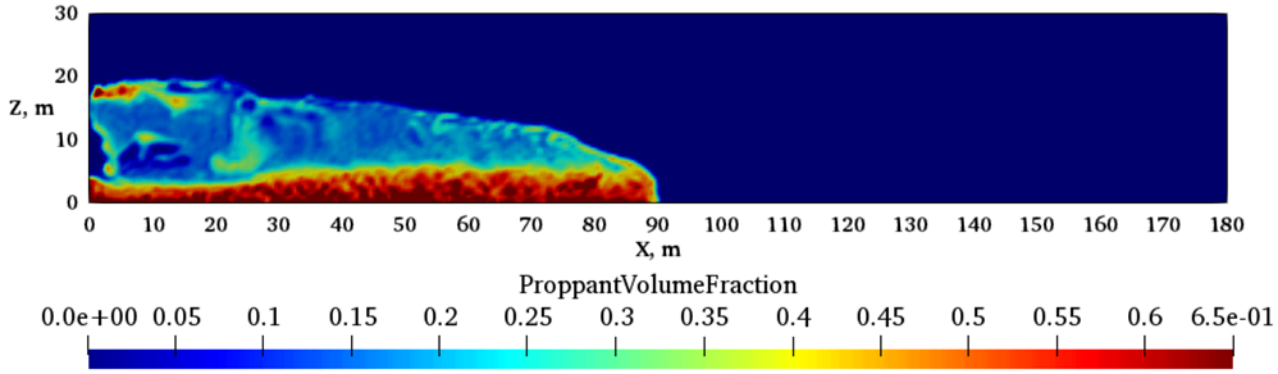

Figure 14. Proppant Transport in the Mid Stage

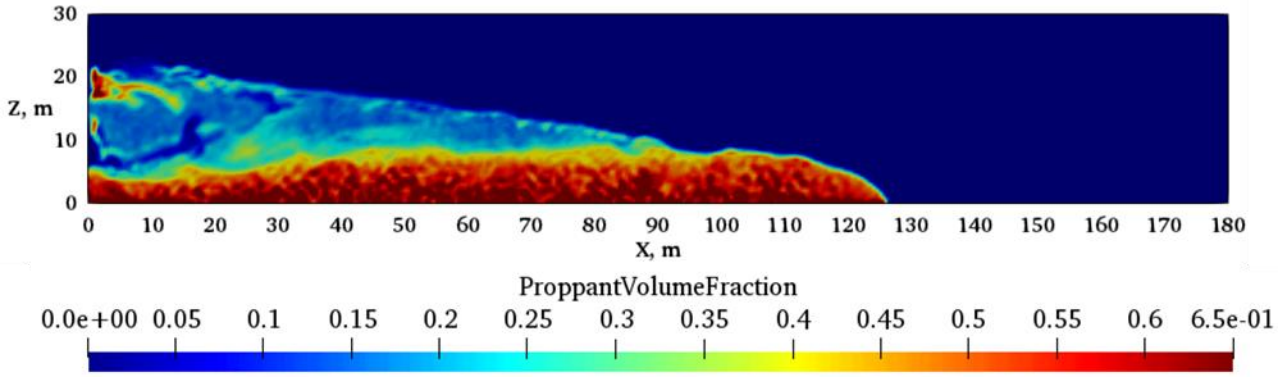

Figure 15. Proppant Transport in the Late Stage

3.3 Case Study 2 – Fracture Height

We investigated the effect of fracture height by applying fractures with different heights. The six different fracture heights are 15, 25, 30, 45, 75, and 90 m. The other parameters can be found in **Table 2** (cases 1-6). **Figures 16-33** include the contour plot of those cases. The final proppant length and suspension area from those figures were estimated by using Image J and listed in **Table 3**. It can be observed that the proppant length is different only for 15 m fracture height for every time step. This observation is consistent with the conclusion of Hu et al. (2018). Proppants injected into a fracture with smaller height has the strongest wash-out effect, in which

the newly injected proppants drove more settled proppants near the injection place to remobilize. Consequently, the proppant length with 15 m fracture height is the largest among these 5 cases, while its proppant settlement near the injection point is the least. On the other hand, once fracture height reaches to a certain value, increasing fracture height is verified to have a negligible impact on both proppant bed height and length. Proppant lengths of 75 and 90 m fracture heights got slightly longer than the base case as the injection proceeds. This result is caused by the influence of the gravity settling effect of particles.

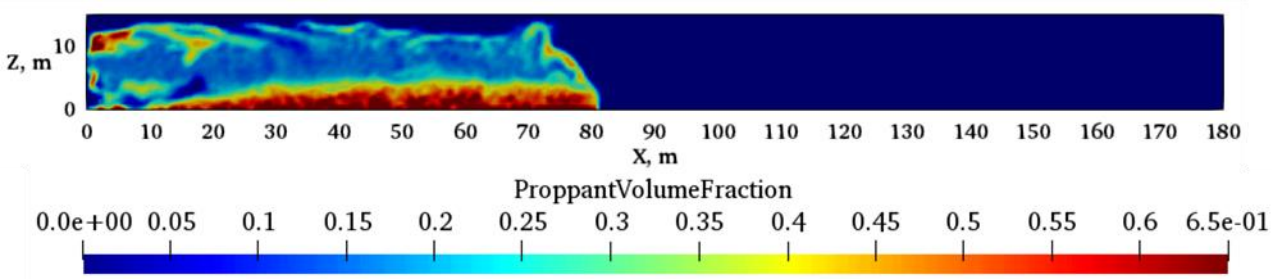

Figure 16. Proppant Volume Fraction Distribution at 10 min for Fracture Height 15 m, Reprinted from Zhang (2020)

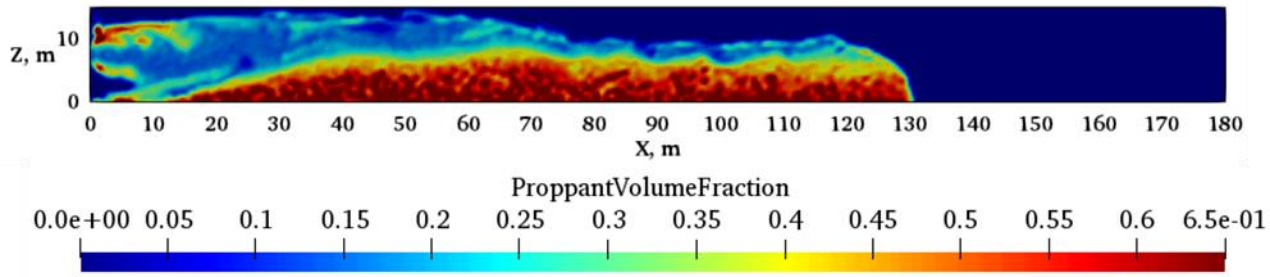

Figure 17. Proppant Volume Fraction Distribution at 20 min for Fracture Height 15 m, Reprinted from Zhang (2020)

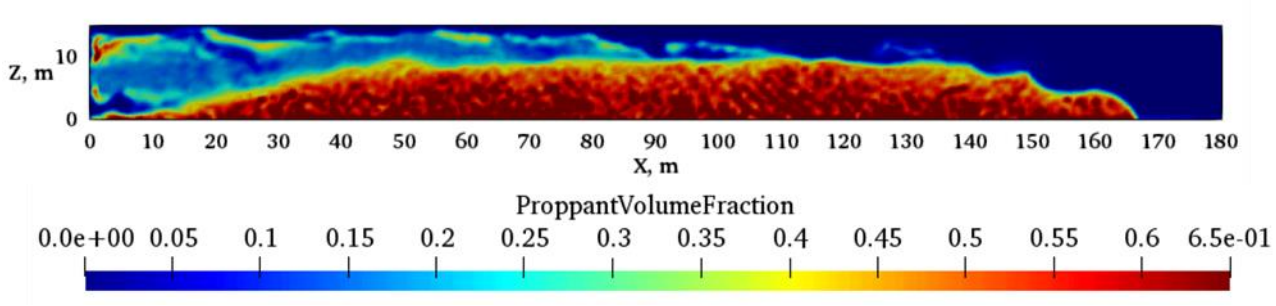

Figure 18. Proppant Volume Fraction Distribution at 30 min for Fracture Height 15 m, Reprinted from Zhang (2020)

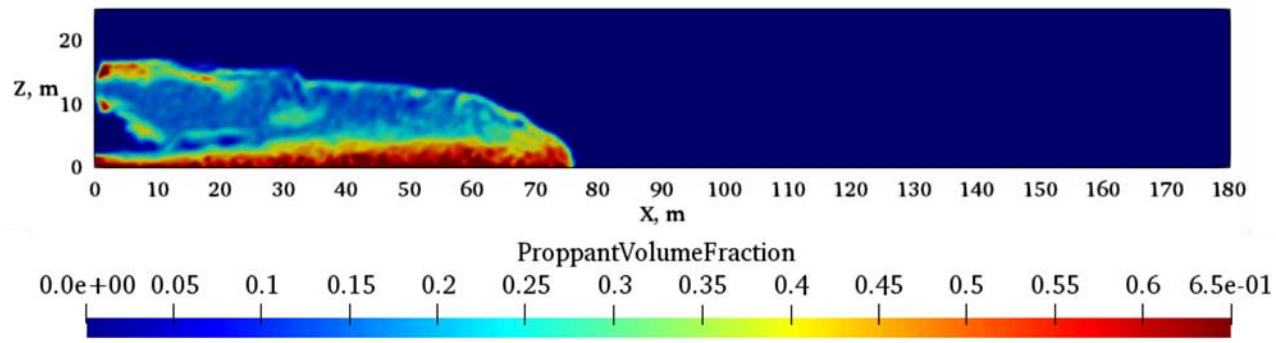

Figure 19. Proppant Volume Fraction Distribution at 10 min for Fracture Height 25 m

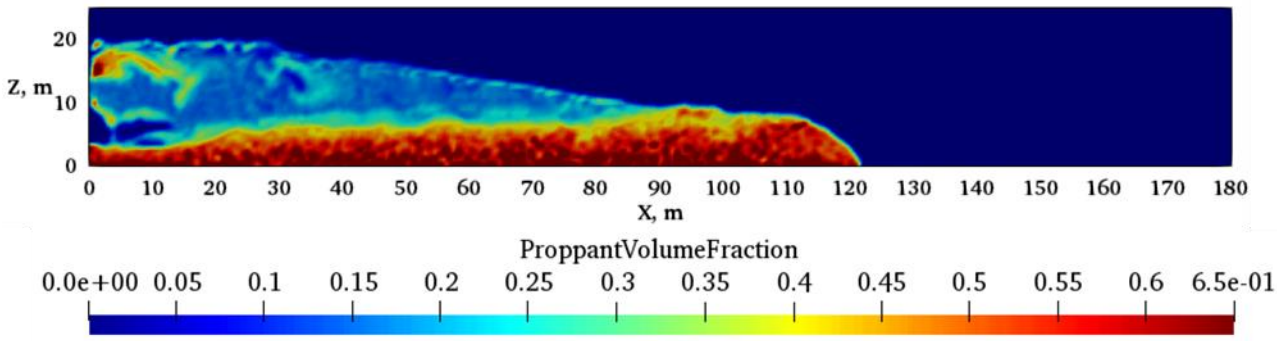

Figure 20. Proppant Volume Fraction Distribution at 20 min for Fracture Height 25 m

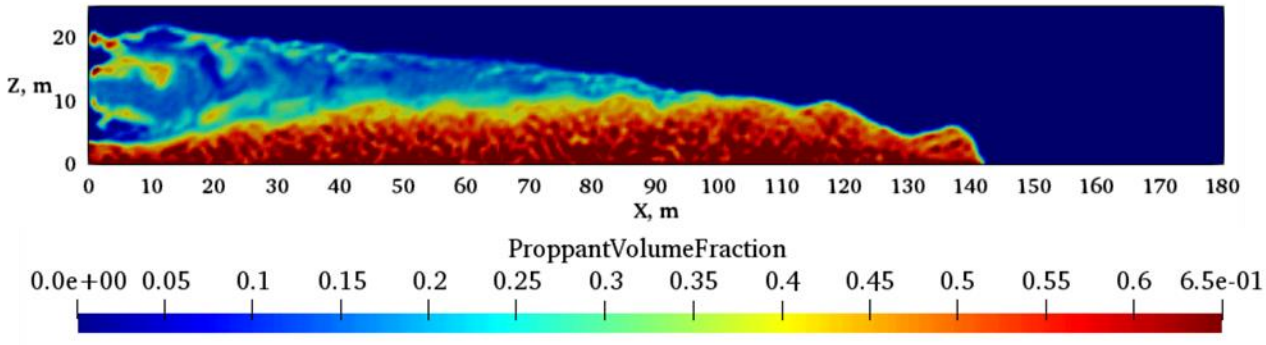

Figure 21. Proppant Volume Fraction Distribution at 30 min for Fracture Height 25 m

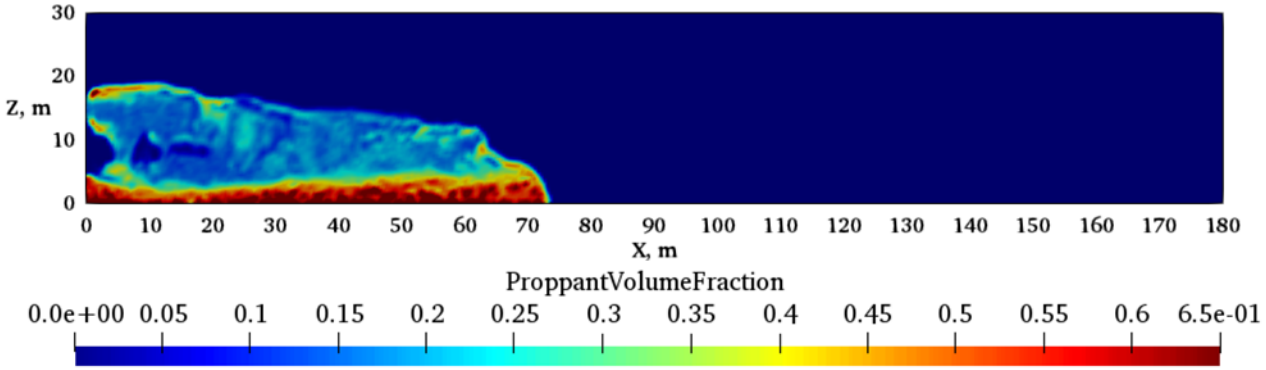

Figure 22. Proppant Volume Fraction Distribution at 10 min for Fracture Height 30 m, Reprinted from Zhang (2020)

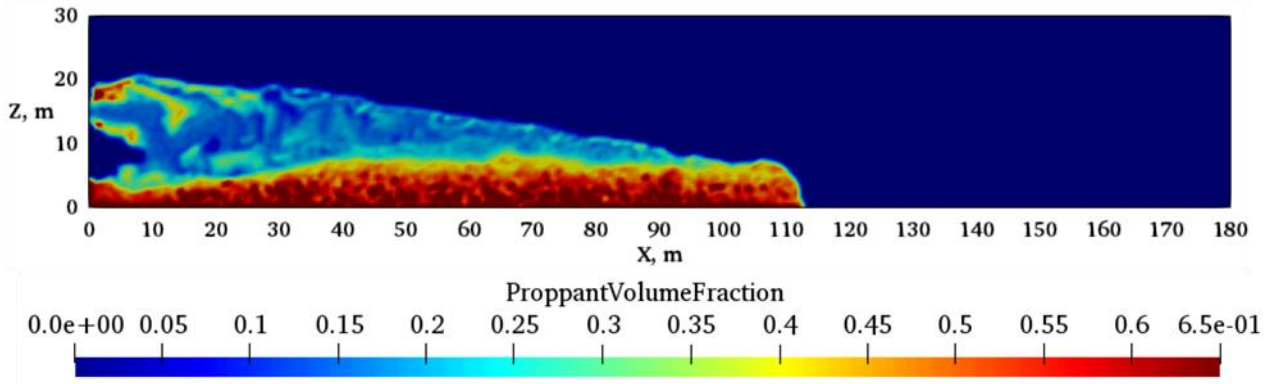

Figure 23. Proppant Volume Fraction Distribution at 20 min for Fracture Height 30 m, Reprinted from Zhang (2020)

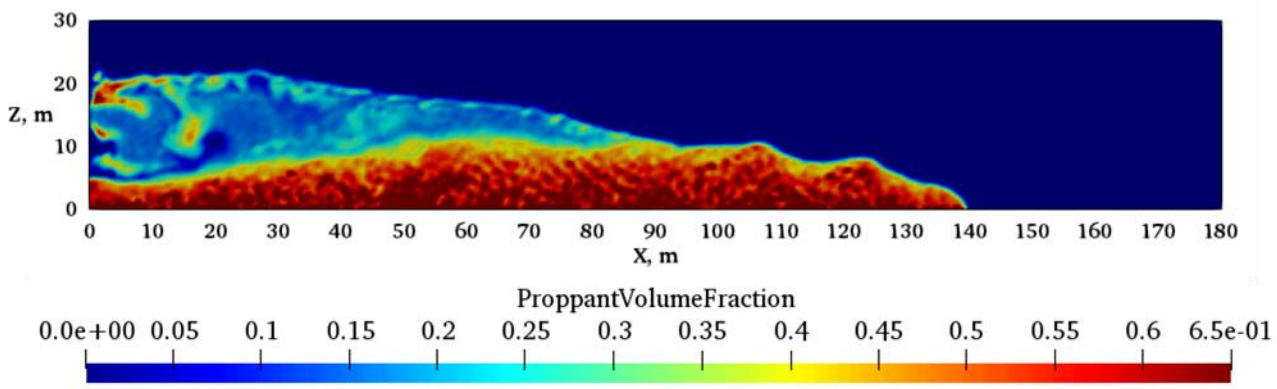

Figure 24. Proppant Volume Fraction Distribution at 30 min for Fracture Height 30 m, Reprinted from Zhang (2020)

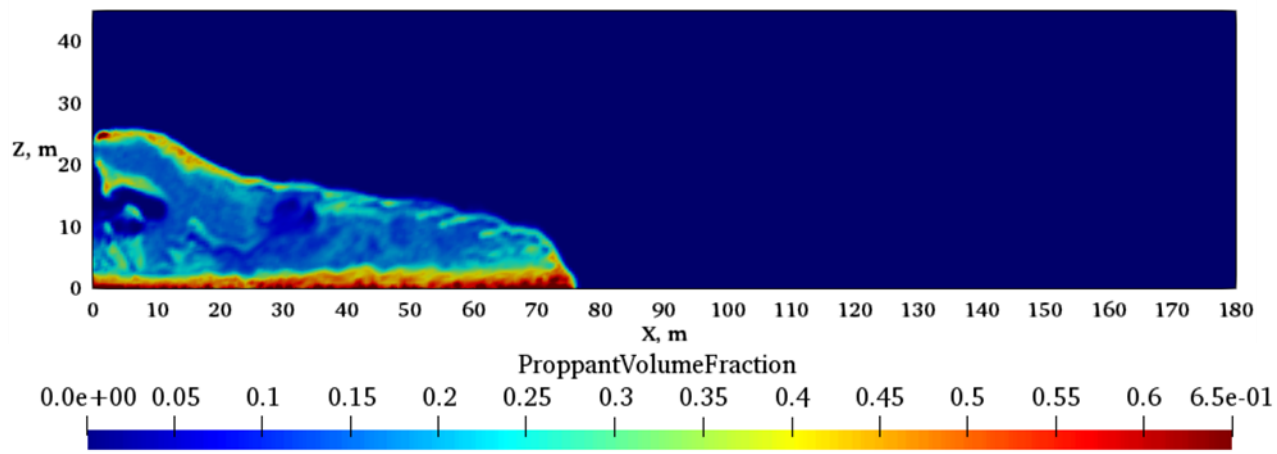

Figure 25. Proppant Volume Fraction Distribution at 10 min for Fracture Height 45 m, Reprinted from Zhang (2020)

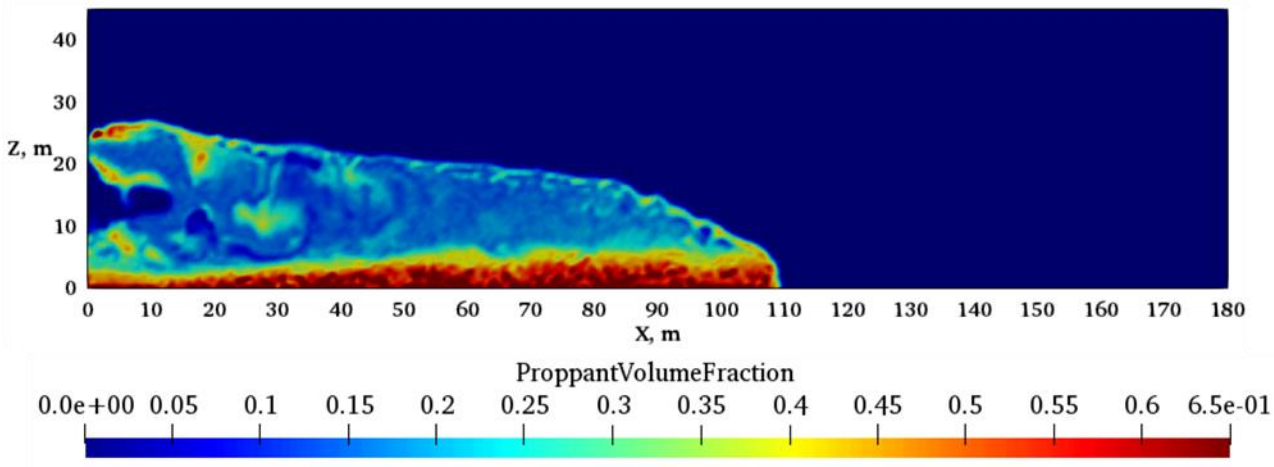

Figure 26. Proppant Volume Fraction Distribution at 20 min for Fracture Height 45 m, Reprinted from Zhang (2020)

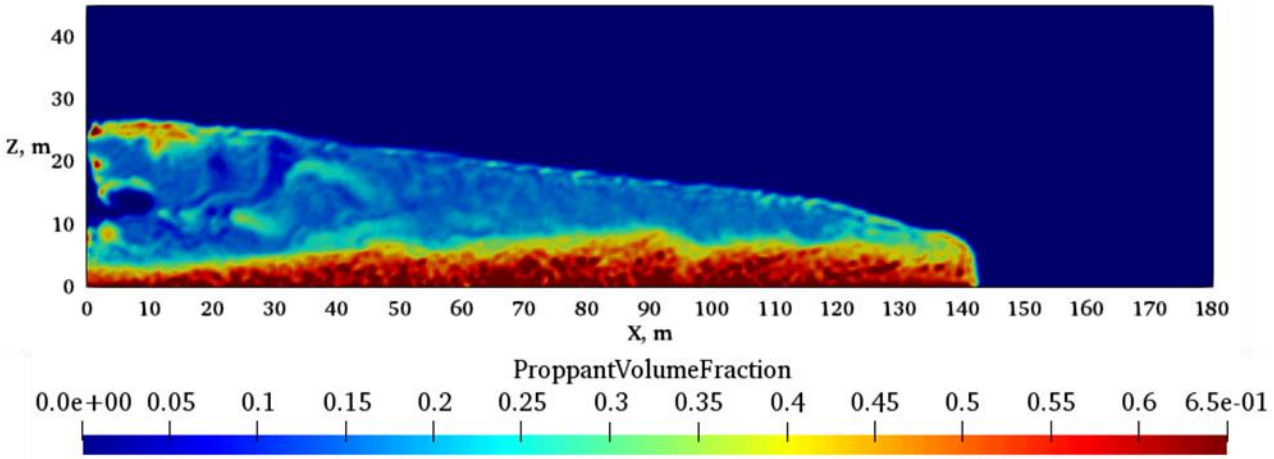

Figure 27. Proppant Volume Fraction Distribution at 30 min for Fracture Height 45 m, Reprinted from Zhang (2020)

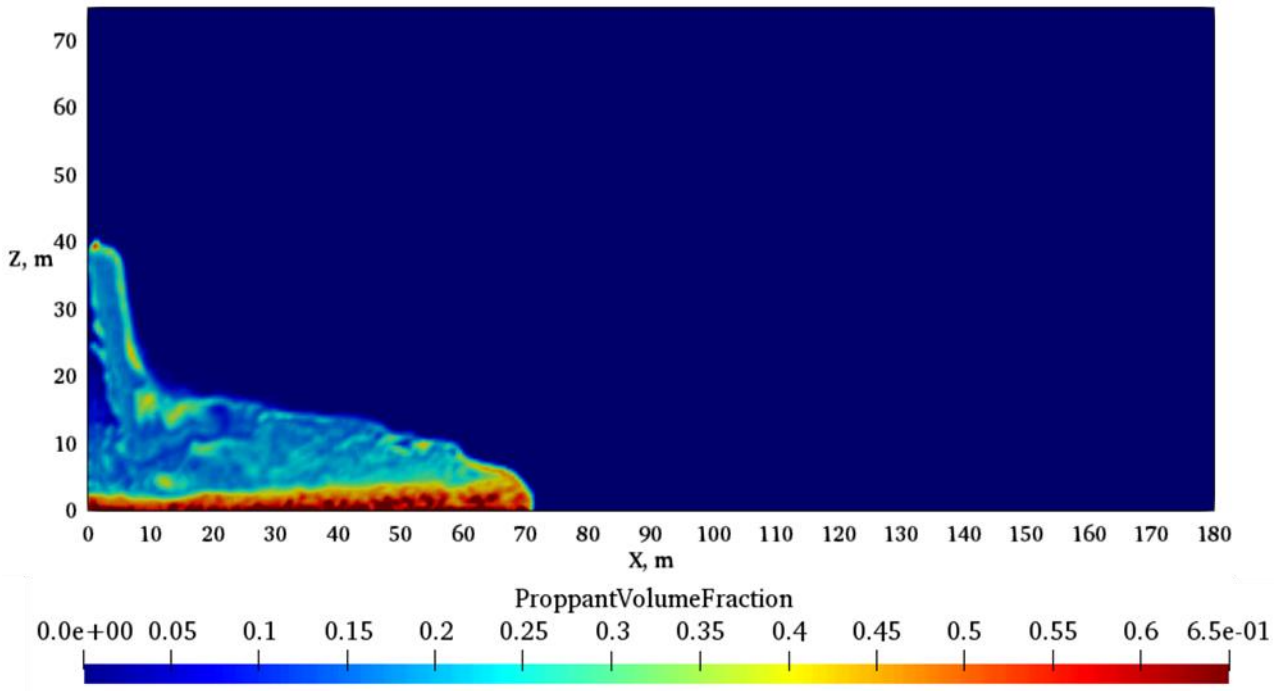

Figure 28. Proppant Volume Fraction Distribution at 10 min for Fracture Height 75 m, Reprinted from Zhang (2020)

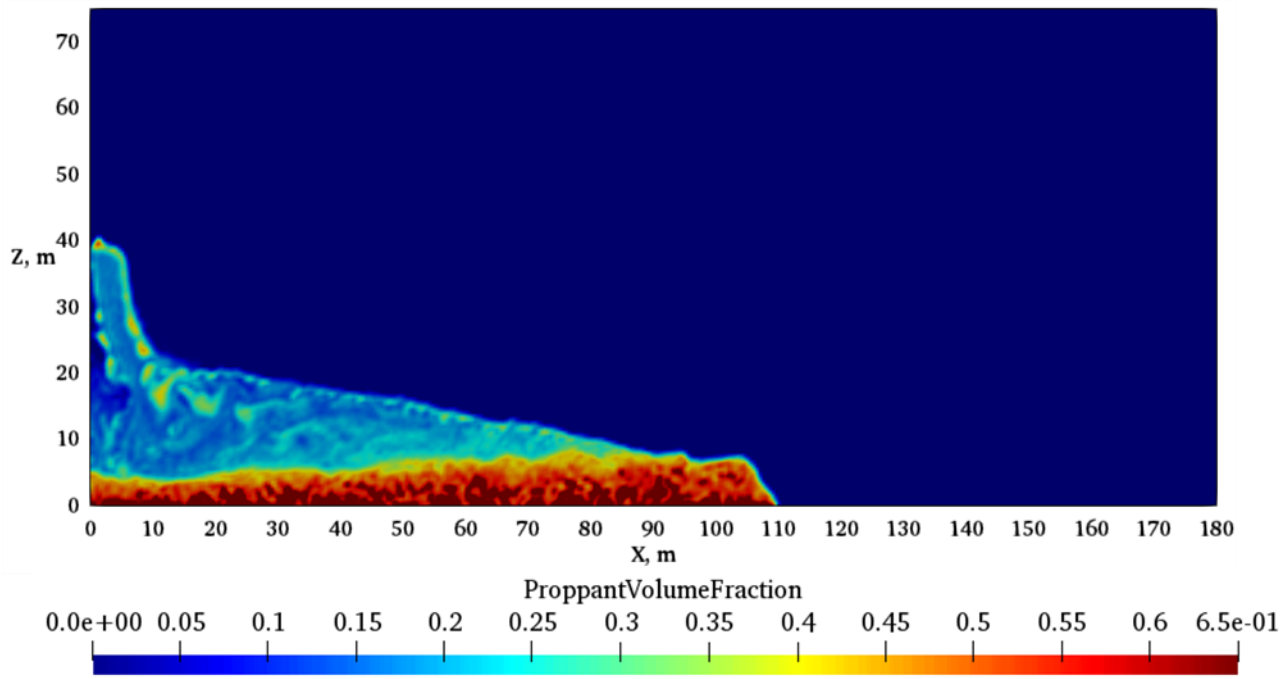

Figure 29. Proppant Volume Fraction Distribution at 20 min for Fracture Height 75 m, Reprinted from Zhang (2020)

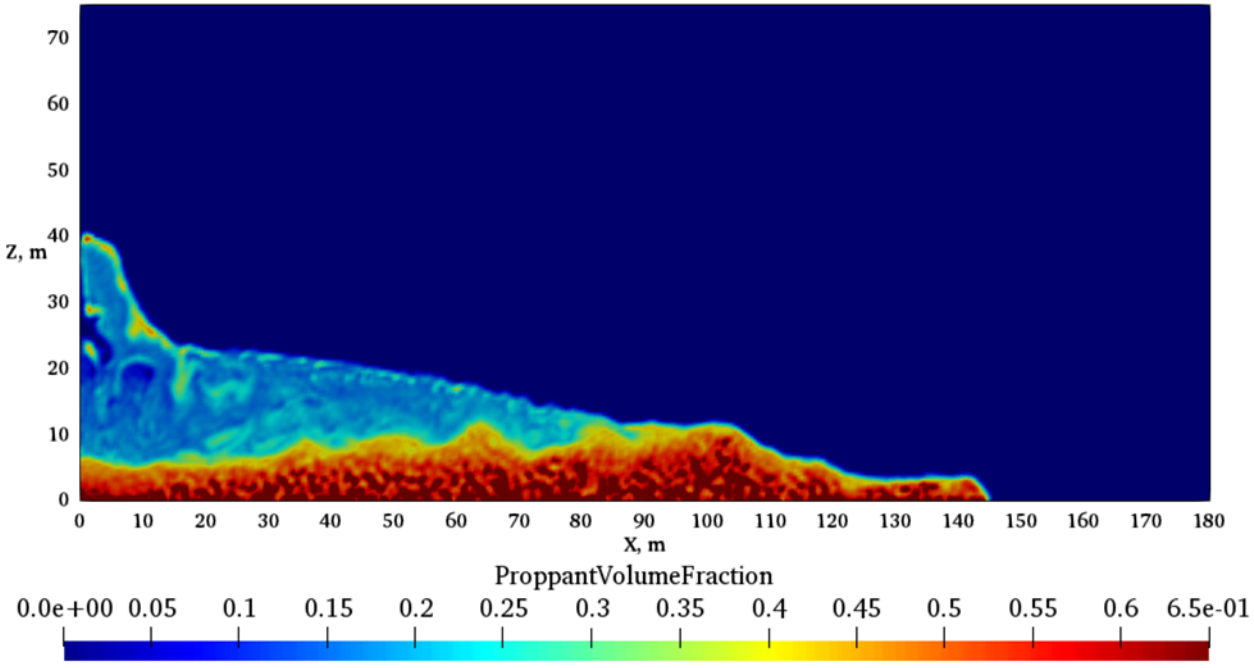

Figure 30. Proppant Volume Fraction Distribution at 30 min for Fracture Height 75 m, Reprinted from Zhang (2020)

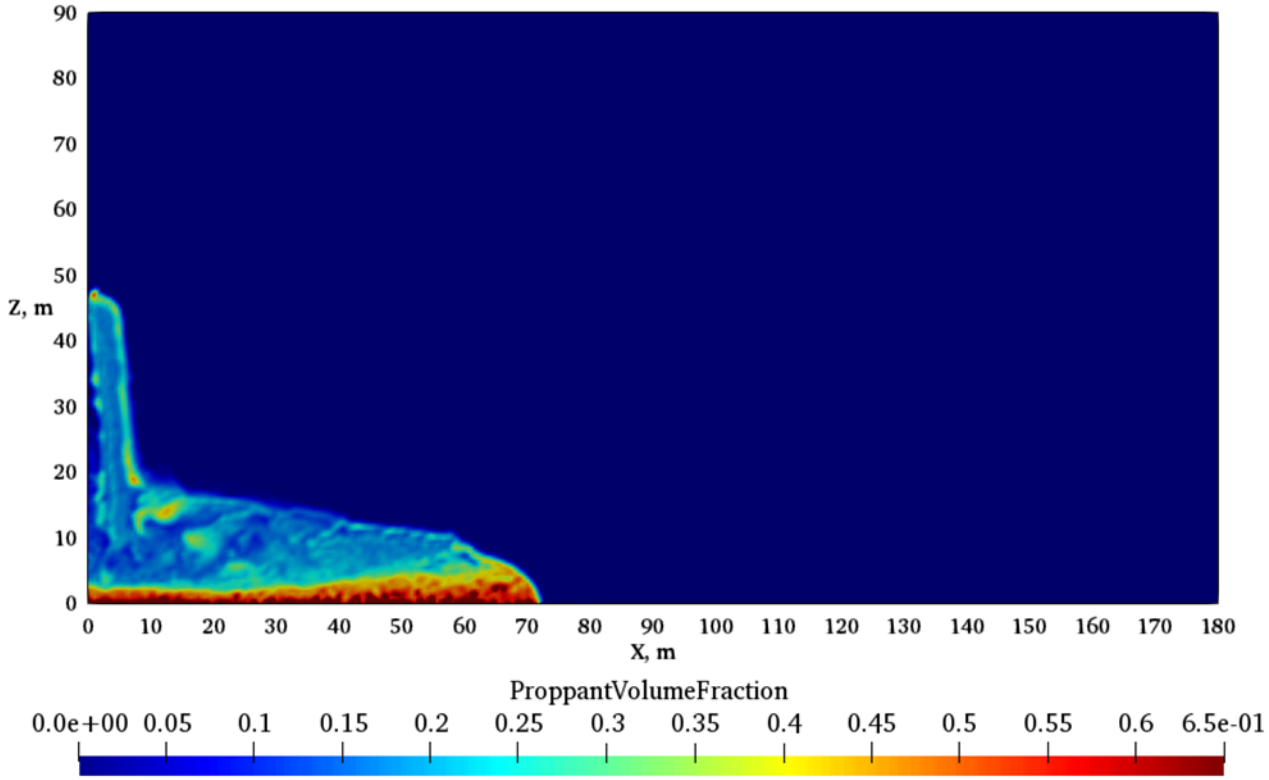

Figure 31. Proppant Volume Fraction Distribution at 10 min for Fracture Height 90 m, Reprinted from Zhang (2020)

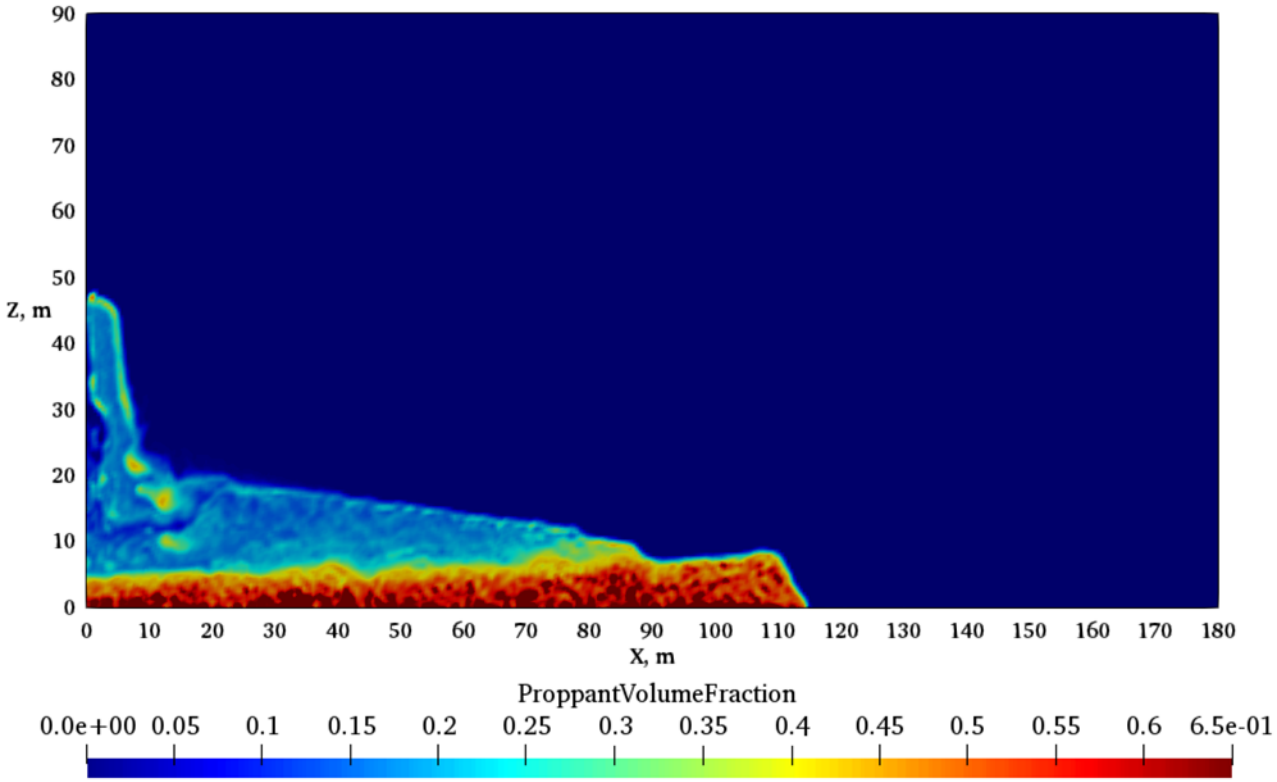

Figure 32. Proppant Volume Fraction Distribution at 20 min for Fracture Height 90 m, Reprinted from Zhang (2020)

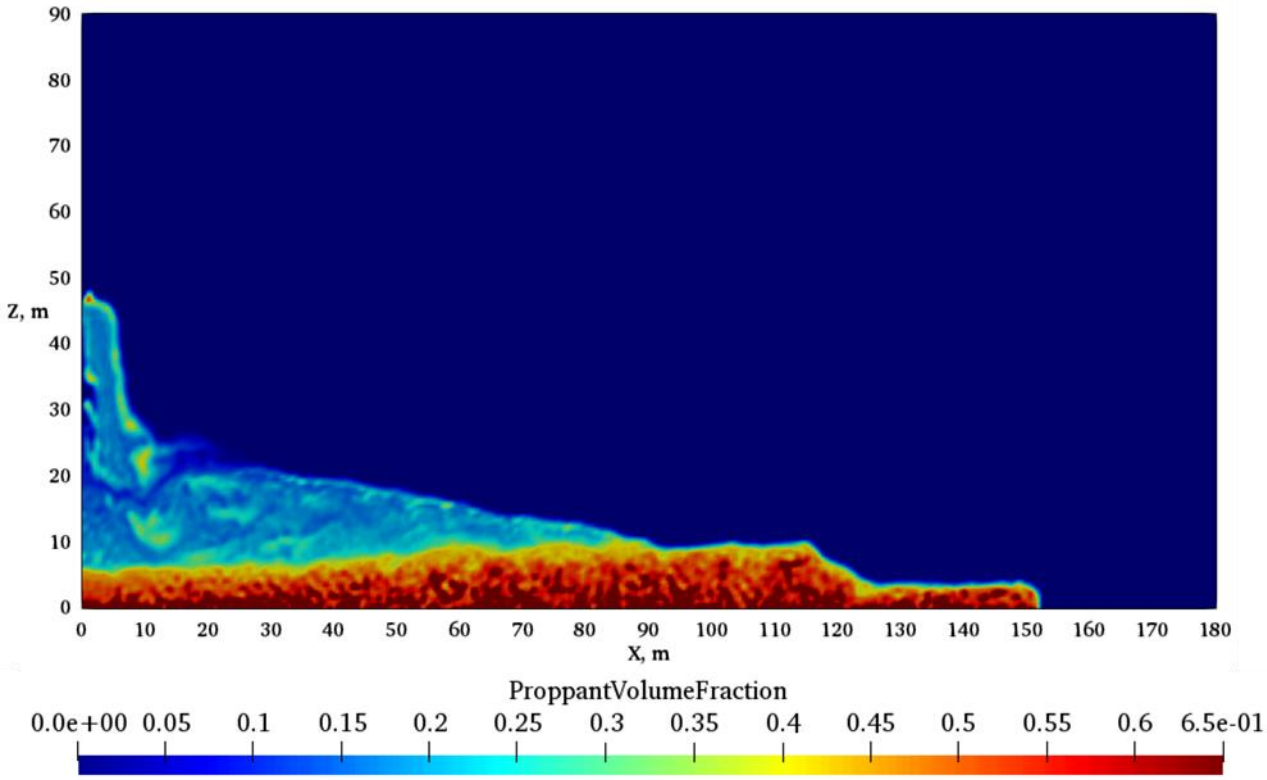

Figure 33. Proppant Volume Fraction Distribution at 30 min for Fracture Height 90 m, Reprinted from Zhang (2020)

Table 3. Effects of Fracture Height on the Proppant Distribution

Fracture Heights	15 m	25 m	30 m	45 m	75 m	90 m
Proppant Suspended (m^2)	520	830	792	1715	771	800
Proppant Length (m)	165.9	141.9	139.3	141.7	144	151

Figures 34-39 provide the age plot of proppant distribution for each fracture height after 30 min injection. The warmer colors in the figures represent the proppant injected earlier, and the proppant injected later is in colder colors. Results from figures confirmed the association between small fracture height and stronger wash-out effect. According to **Figures 34-36**, the old

proppant mixed with following newly injected proppant and transported near the outlet. Moreover, this effect can be mitigated by increasing fracture height. It can be seen in **Figures 37-39** that the proppant injected earlier and the newly injected proppant were layered with fracture heights of 45 m, 75 m, 90 m. We drew the particle settling velocity for 15 m fracture height to investigate the mechanism further. As is shown in **Figure 40**, the proppants gained larger settling velocity (shown in red) from their collision with the top layer of fracture and washed more proppant to the end of fracture. This result would explain the nearly unchanging proppant length under the effect of stronger wash-out in 25 m fracture height.

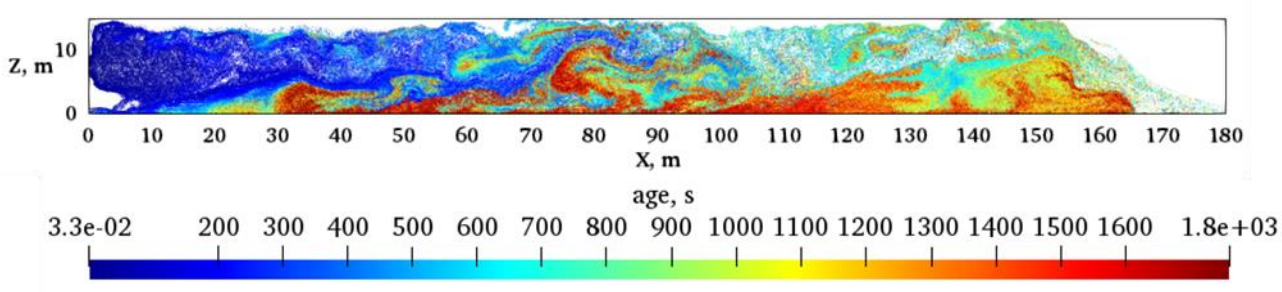

Figure 34. Age Plot of Proppant Distribution at 30 min for Fracture Height 15 m

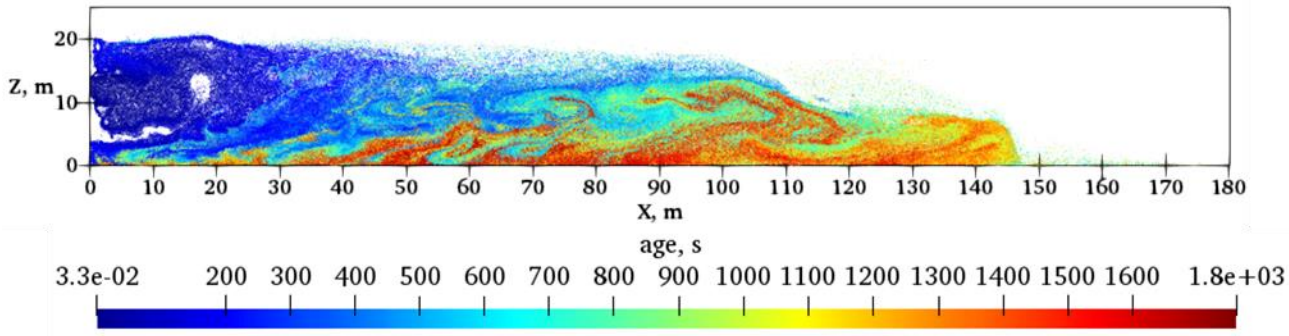

Figure 35. Age Plot of Proppant Distribution at 30 min for Fracture Height 25 m

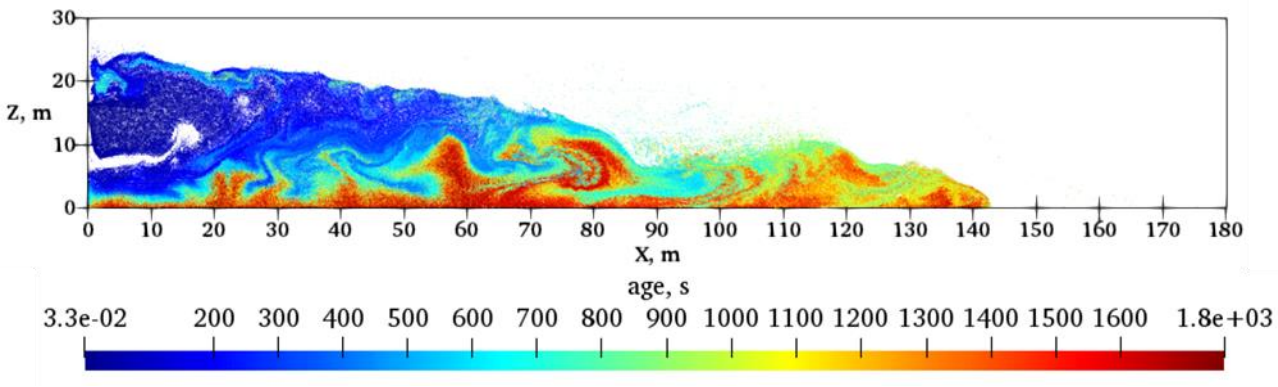

Figure 36. Age Plot of Proppant Distribution at 30 min for Fracture Height 30 m

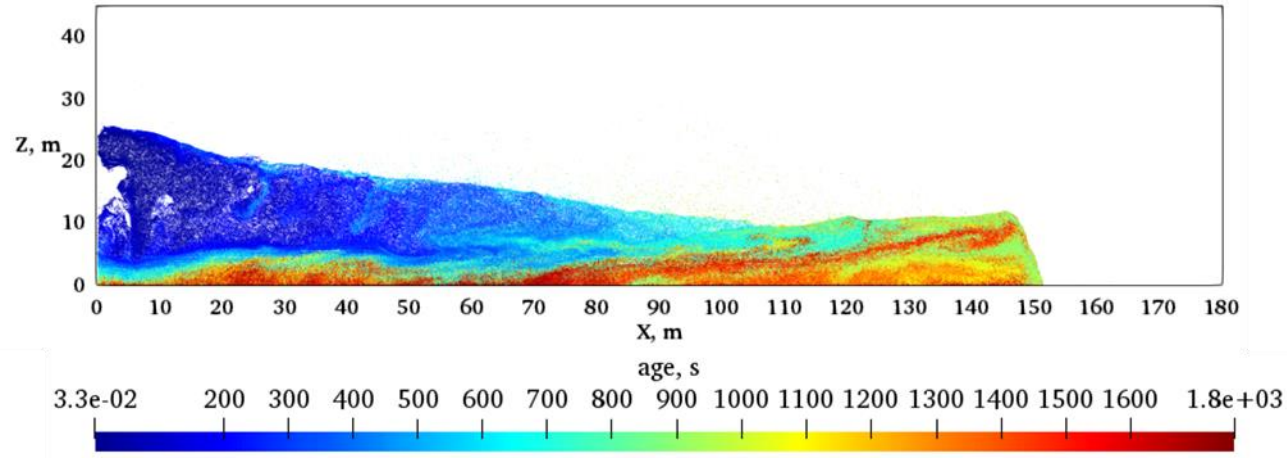

Figure 37. Age Plot of Proppant Distribution at 30 min for Fracture Height 45 m

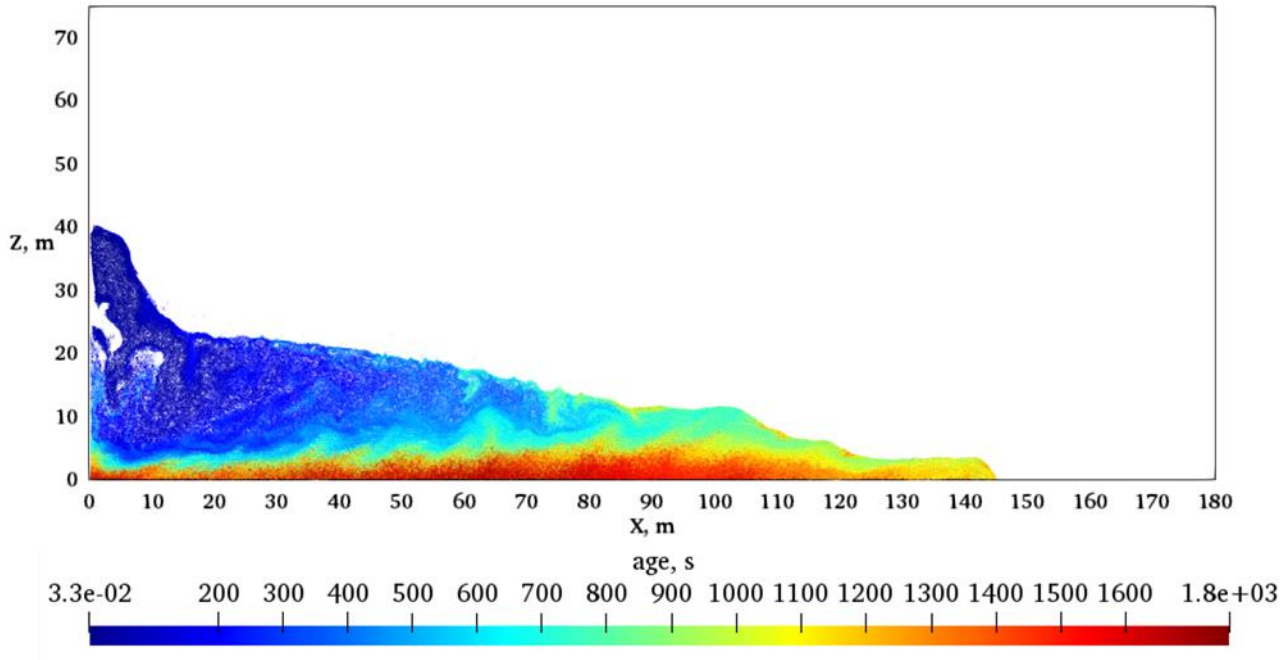

Figure 38. Age Plot of Proppant Distribution at 30 min for Fracture Height 75 m

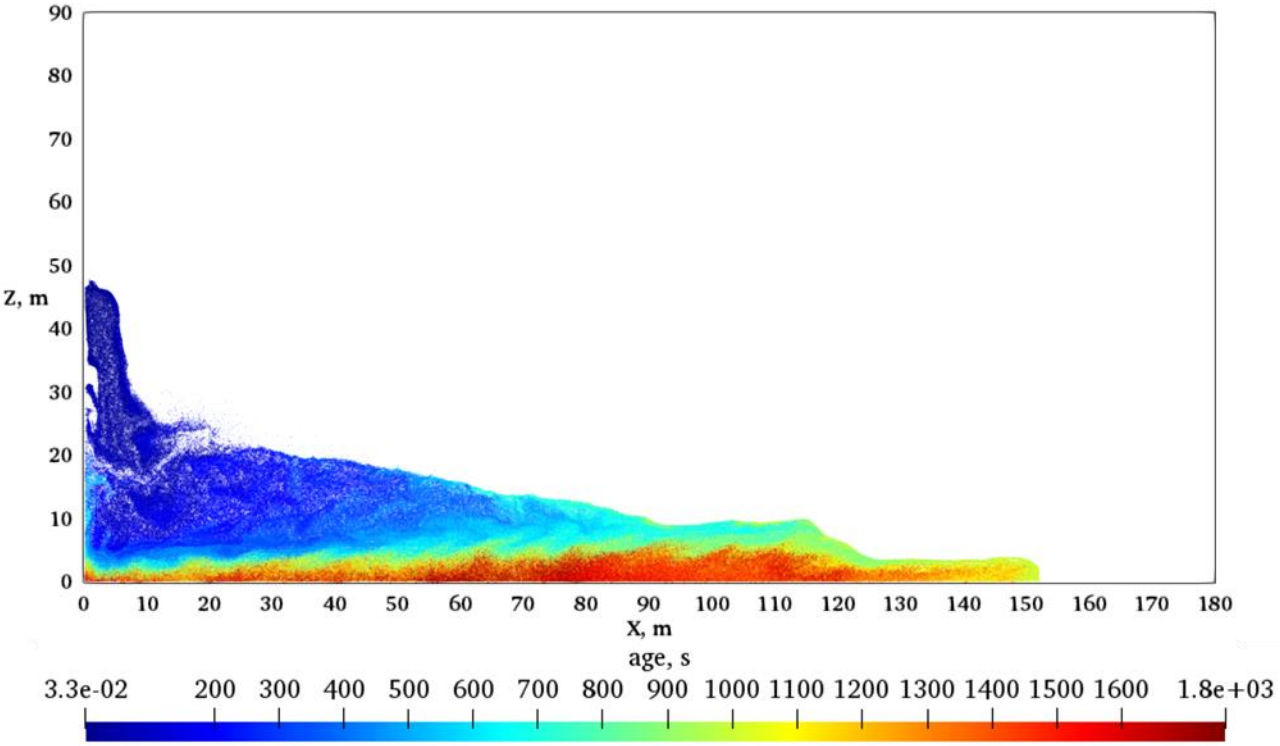

Figure 39. Age Plot of Proppant Distribution at 30 min for Fracture Height 90 m

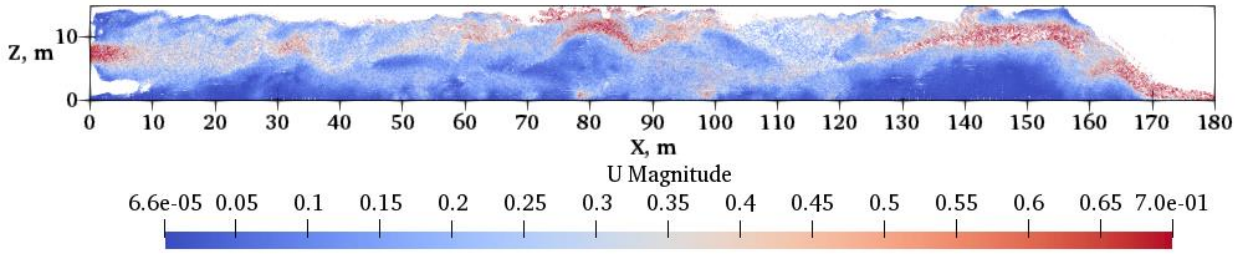

Figure 40. Particle Settling Velocity at 30 min for Fracture Height 15 m

3.4 Case Study 3 – Fluid Viscosity

It is commonly known that fluid viscosity is a key parameter affecting proppant transport. Since proppant placement is sensitive to the fluid viscosity, it is necessary to understand the role of fluid viscosity in proppant distribution. The following case study is designed to verify the effect of fluid viscosity. Five additional cases (cases 7-11) are fluid viscosity of 0.5, 2, 3, 10, 30 cp. The fluid viscosity of slickwater can be affected by both the reservoir pressure and temperature, and the first three cases (cases 7, 8, 9) were designed for this reason. The other two cases (cases 10 and 11) were constructed in aim to know the proppant transport behavior in a high viscosity fluid.

Figures 41-46 show the simulation results after 30 mins injection. Since the significant difference is shown from the results, the evolution of proppant volume fraction was not displayed in this investigation. The magnitudes of the final proppant length and suspension area are collected in **Table 4**. It can be seen that with the increase of fluid viscosity, the proppant bed height decreases significantly. At the same time, the lateral length of proppant bed firstly slightly decreases and then increases. After that, there was less proppant settlement with fluid viscosity of 30 cp (**Figure 46**). The reason is that increasing fluid viscosity can decrease the fluid Reynold number, and the viscous force will become dominant. As a result, more proppants were suspended, and the interactions of particles decrease. With proppant suspension expanding, proppant bed length

decreases (**Figures 43 and 44**). As we kept increasing the viscosity to 10 cp, the flow would be closer to laminar, and the proppant bed would directly reach fracture length. With 30 cp fluid, very less proppant settled after 30 mins injection because proppants were suspended in the entire fracture.

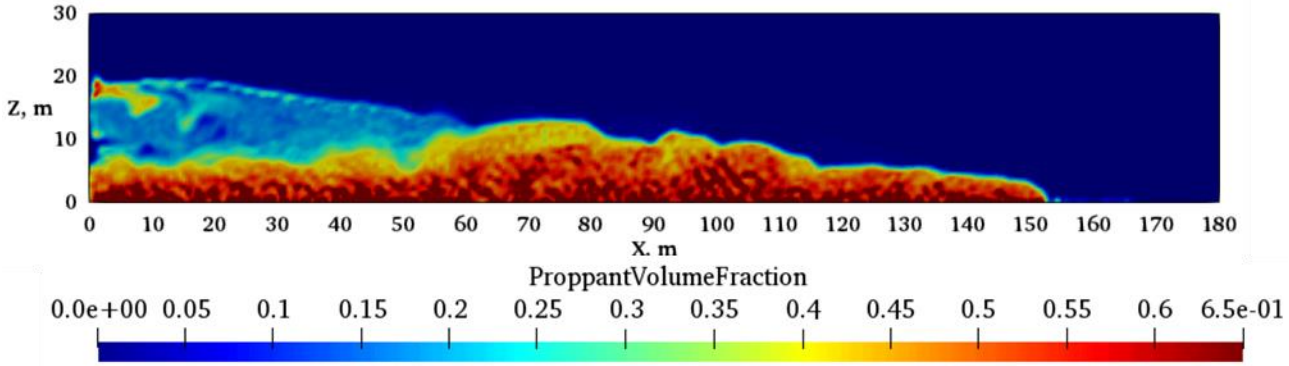

Figure 41. Proppant Volume Fraction Distribution at 30 min for Fluid Viscosity 0.5 cp, Reprinted from Zhang (2020)

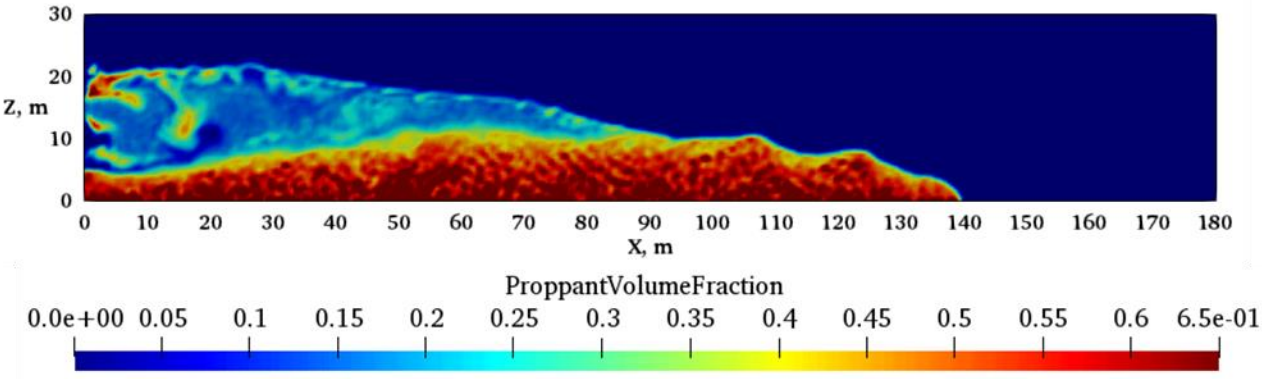

Figure 42. Proppant Volume Fraction Distribution at 30 min for Fluid Viscosity 1 cp, Reprinted from Zhang (2020)

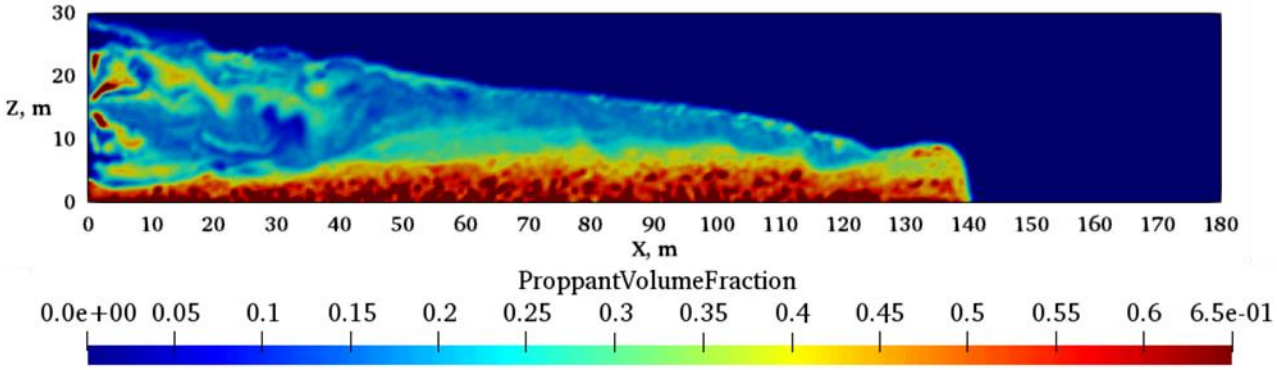

Figure 43. Proppant Volume Fraction Distribution at 30 min for Fluid Viscosity 2 cp, Reprinted from Zhang (2020)

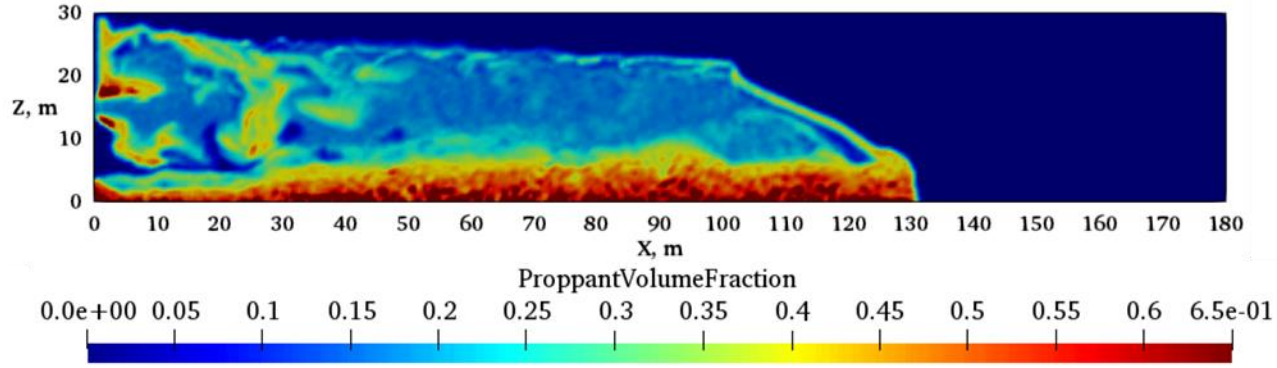

Figure 44. Proppant Volume Fraction Distribution at 30 min for Fluid Viscosity 3 cp, Reprinted from Zhang (2020)

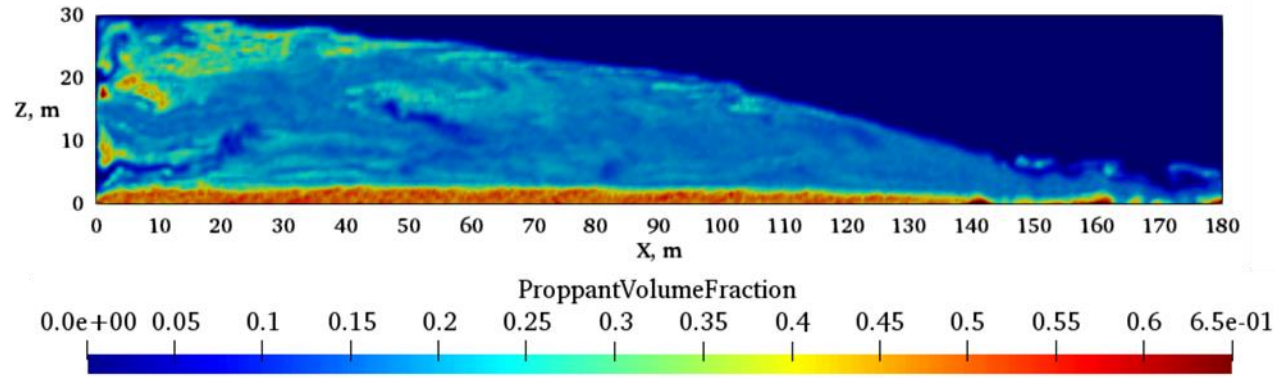

Figure 45. Proppant Volume Fraction Distribution at 30 min for Fluid Viscosity 10 cp, Reprinted from Zhang (2020)

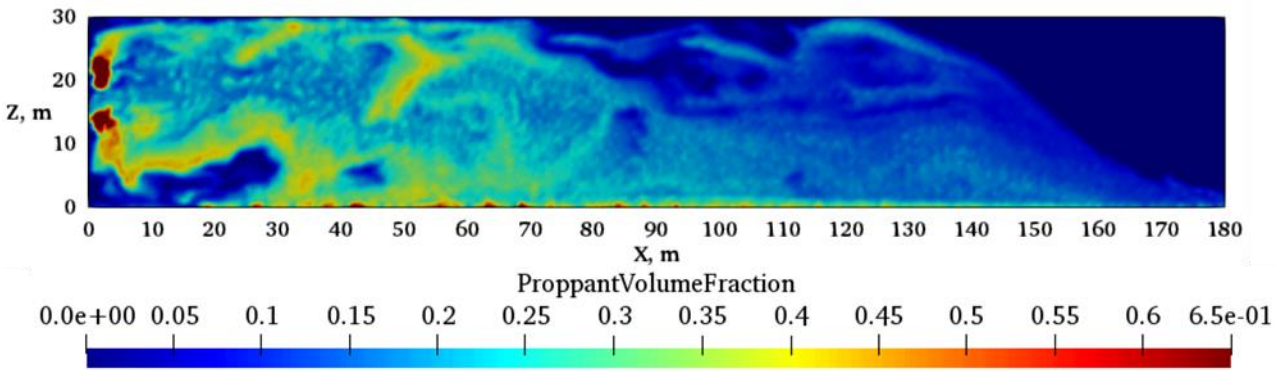

Figure 46. Proppant Volume Fraction Distribution at 30 min for Fluid Viscosity 30 cp, Reprinted from Zhang (2020)

Table 4. Effects of Fluid Viscosity on the Proppant Distribution

Fluid Viscosities	0.5 cp	1 cp	2 cp	3 cp	10 cp	30 cp
Proppant Suspended (m^2)	504	865	1442	1985	2777	4153
Proppant Length (m)	152.5	139.2	139.6	130.5	180	

3.5 Case Study 4 – Proppant Concentration

Investigate the effect of proppant concentration and injection rate with the same injection time is the typical approach applied in previous studies. For example, the higher injection rate was applied in the simulation with more proppants injected. Even though it is realistic in the field due to the low cost of sand, this approach ignored the influence of different proppant volumes. To address this concern, when we varied the proppant concentrations in case 12 (1.5lb/gal) and case 13 (2.5 b/gal), the injection times were normalized for the same injected proppant volume. This

proppant volume can be calculated based on the injection condition and fracture geometry in the base case, which is 6.5 m^3.

Figures 47-49 and **Figures 56-58** present a comparison between proppant distribution with different proppant concentrations at the same injection time and normalized injection time. It can be noticed that at the same injection time, high concentration slurry settled faster to reach the proppant equilibrium height. This observation was consistent with previous studies. However, for the normalized injection duration, the proppant length decreases as the proppant concentration increases, and the proppant bed height has rarely changed.

Figures 50-58 show the evolution of proppant distribution at 0.3, 0.5, 1.0 of normalized injection time for three different proppant concentrations. According to the figures, the proppant bed length with higher concentration was firstly less than the base case and then arrived at the same distance. This is because more proppants would be injected at each time step for higher proppant concentration. Proppants firstly reached the equilibrium height around the injection point and then traveled in a distance by wash out. On the other hand, for low proppant concentration, it would be easier for the fluid to carry fewer proppants at each time step to the end of fracture. This explanation is in agreement with results obtained in the age plot for each case with various proppant concentrations (**Figures 59-61**). As is shown in the figures, the old proppant with lower concentration was transported and distributed near the outlet. When increasing the concentration, a few oldest proppants settled near the injection point, and the following injected proppants transported some earlier injected proppant to place further. As a result, early injected proppants tend to distribute evenly in the lower region of fracture.

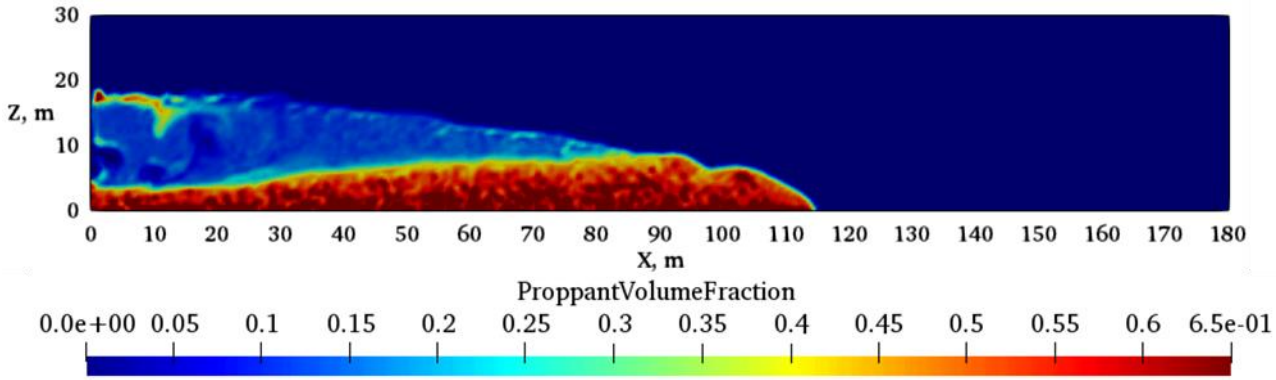

Figure 47. Proppant Volume Fraction Distribution at 24 min for Proppant Concentration 1.5 lb/gal

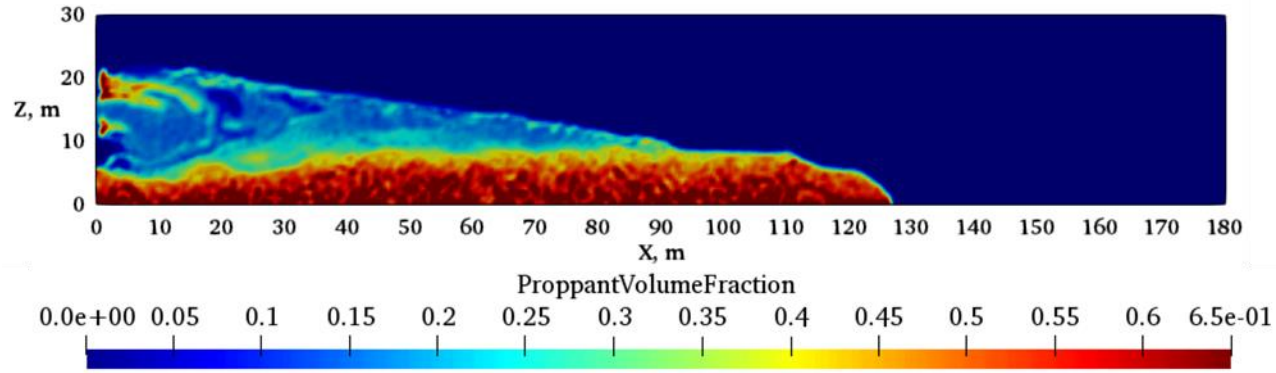

Figure 48. Proppant Volume Fraction Distribution at 24 min for Proppant Concentration 2 lb/gal

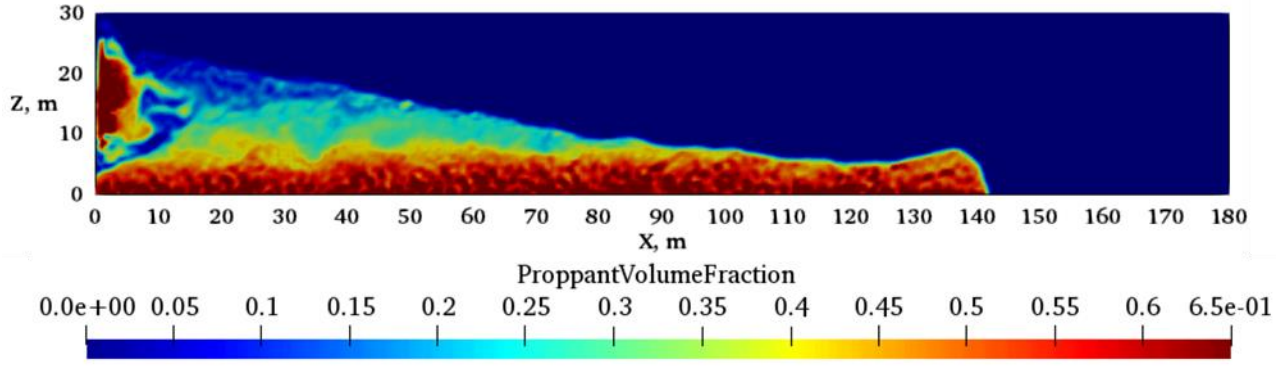

Figure 49. Proppant Volume Fraction Distribution at 24 min for Proppant Concentration 2.5 lb/gal

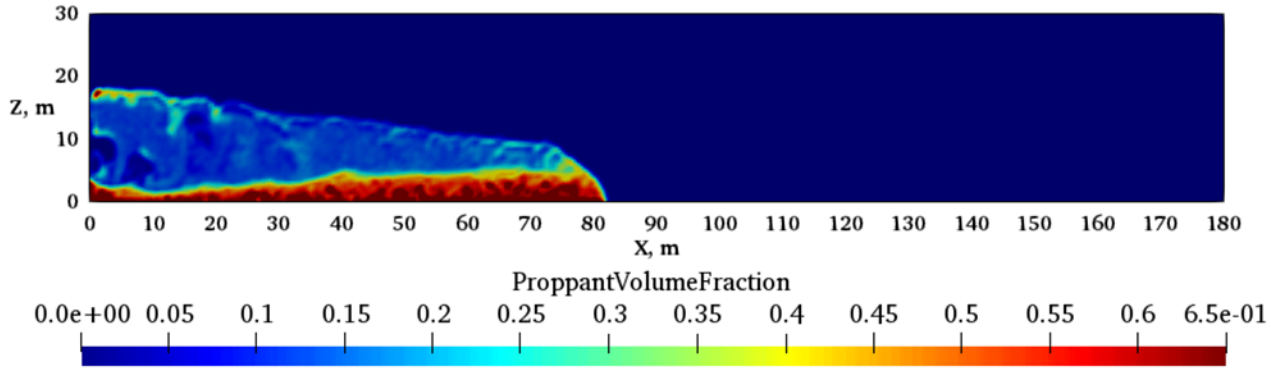

Figure 50. Proppant Volume Fraction Distribution at 13 min for Proppant Concentration 1.5 lb/gal

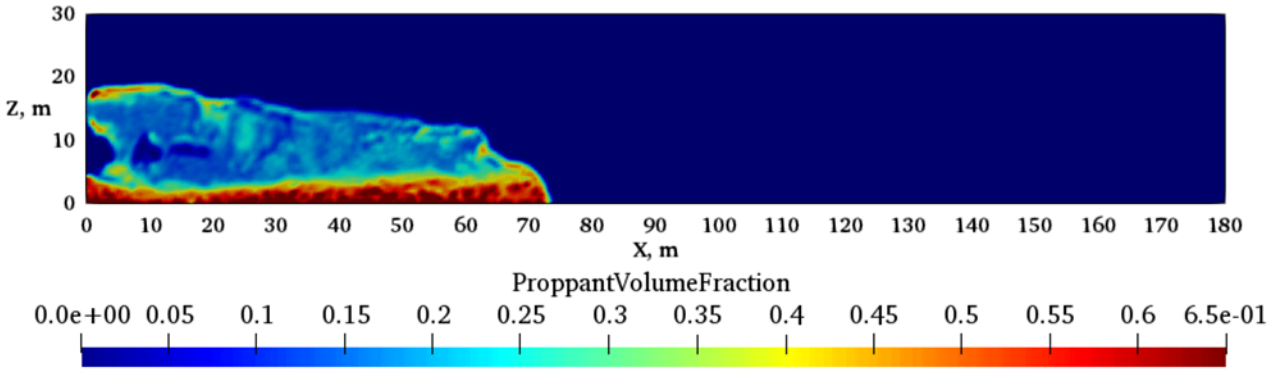

Figure 51. Proppant Volume Fraction Distribution at 10 min for Proppant Concentration 2 lb/gal

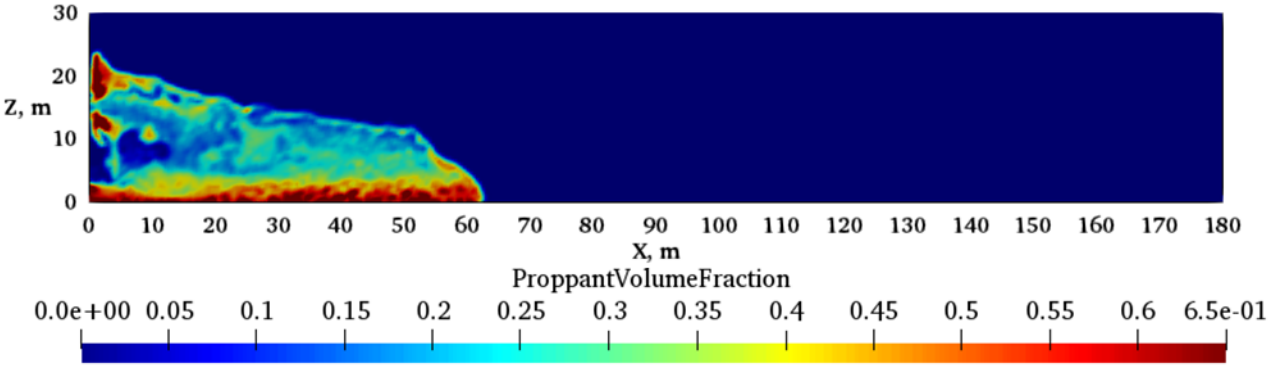

Figure 52. Proppant Volume Fraction Distribution at 8 min for Proppant Concentration 2.5 lb/gal

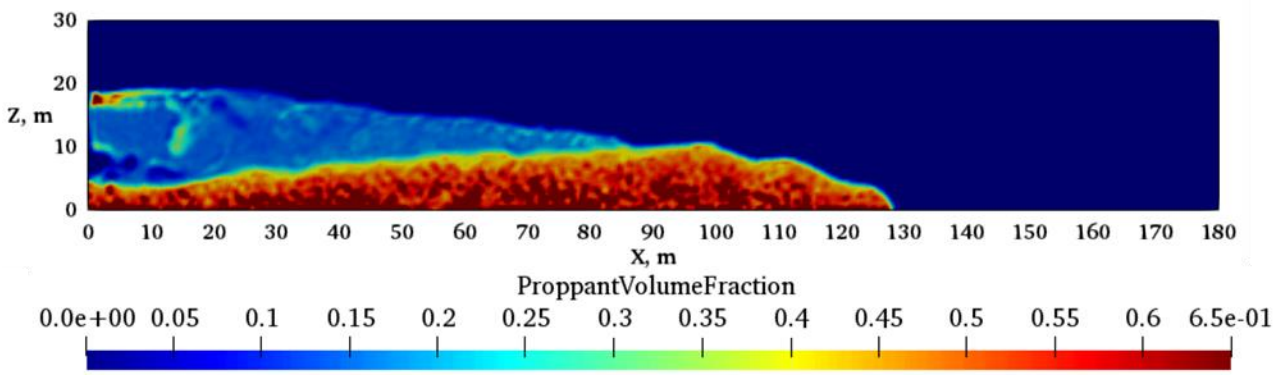

Figure 53. Proppant Volume Fraction Distribution at 20 min for Proppant Concentration 1.5 lb/gal, Reprinted from Zhang (2020)

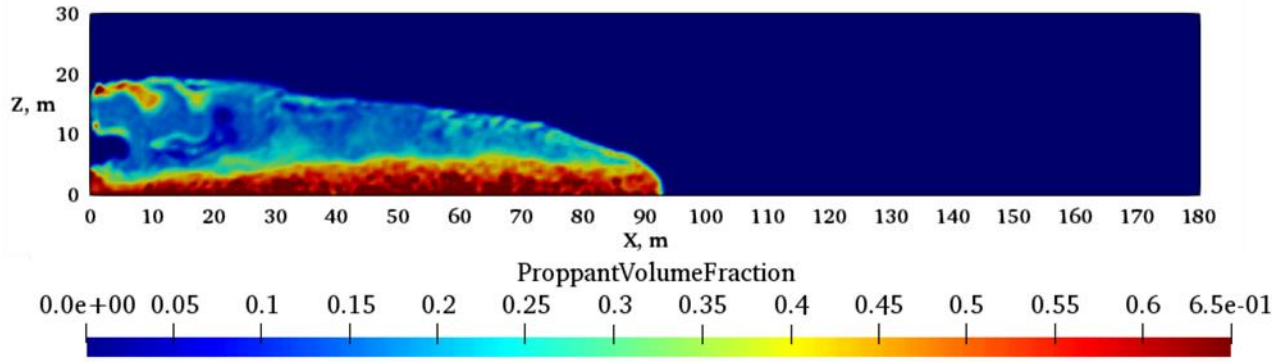

Figure 54. Proppant Volume Fraction Distribution at 15 min for Proppant Concentration 2 lb/gal, Reprinted from Zhang (2020)

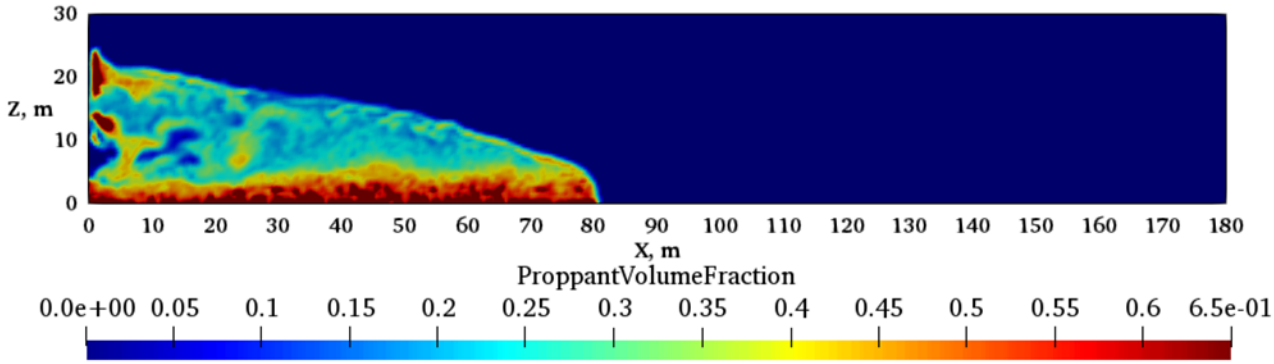

Figure 55. Proppant Volume Fraction Distribution at 12 min for Proppant Concentration 2.5 lb/gal, Reprinted from Zhang (2020)

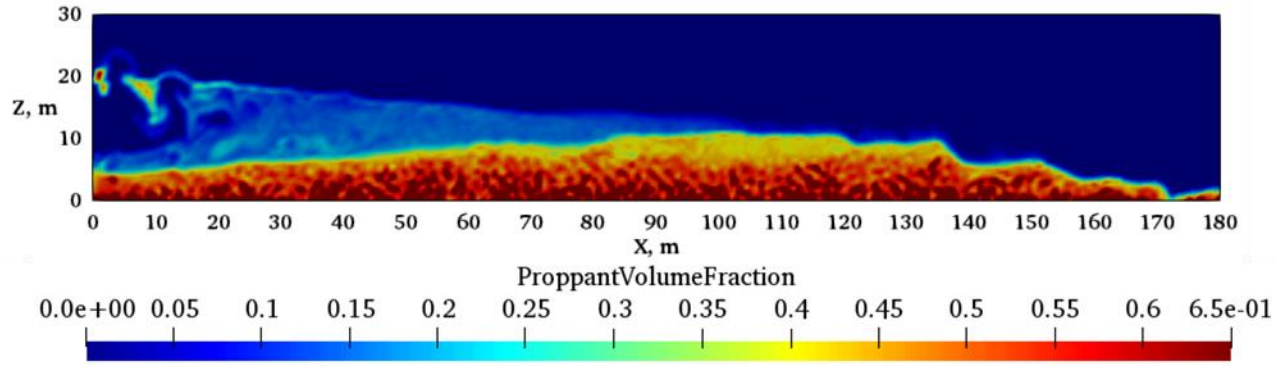

Figure 56. Proppant Volume Fraction Distribution at 40 min for Proppant Concentration 1.5 lb/gal, Reprinted from Zhang (2020)

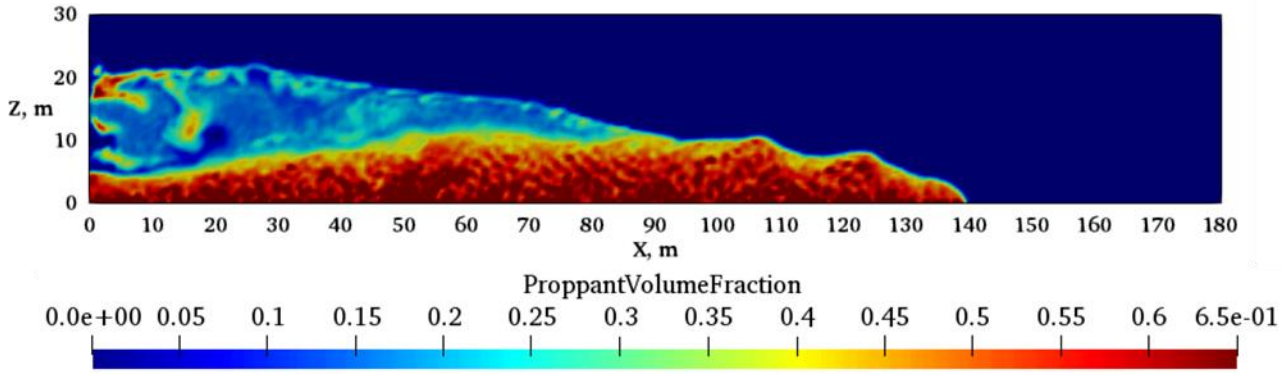

Figure 57. Proppant Volume Fraction Distribution at 30 min for Proppant Concentration 2 lb/gal, Reprinted from Zhang (2020)

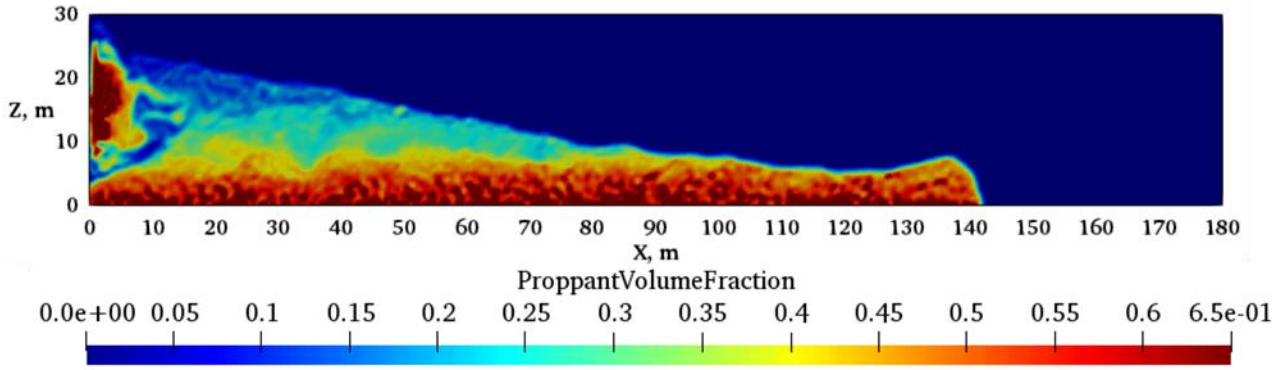

Figure 58. Proppant Volume Fraction Distribution at 24 min for Proppant Concentration 2.5 lb/gal, Reprinted from Zhang (2020)

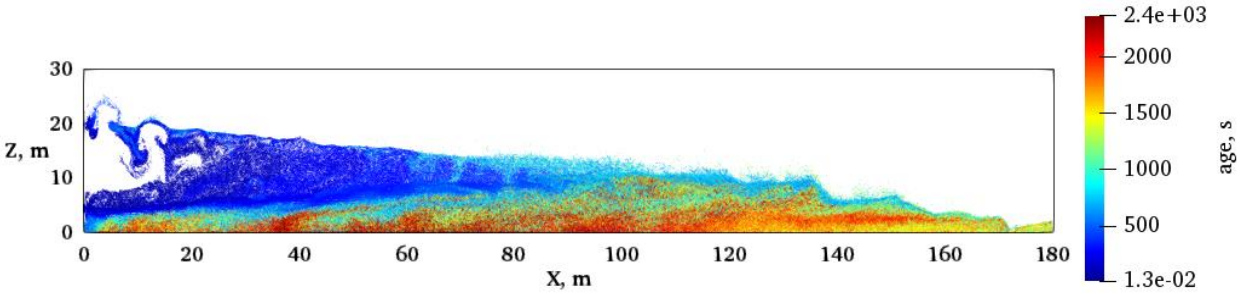

Figure 59. Age Plot of Proppant Distribution at 40 min for Proppant Concentration 1.5 lb/gal

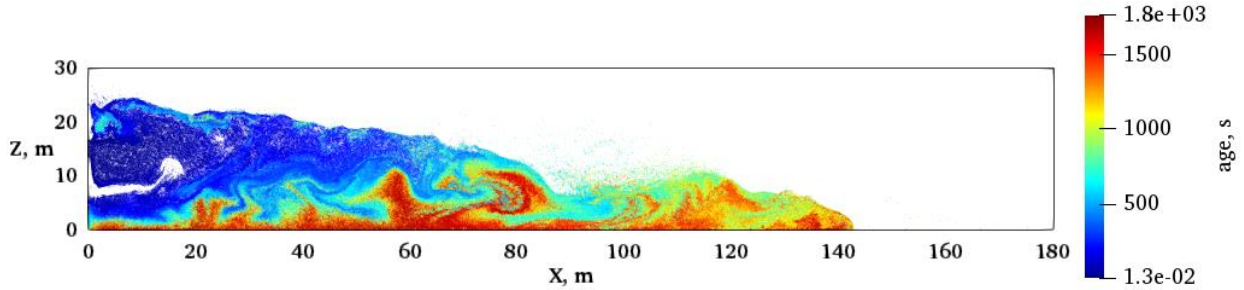

Figure 60. Age Plot of Proppant Distribution at 30 min for Proppant Concentration 2 lb/gal

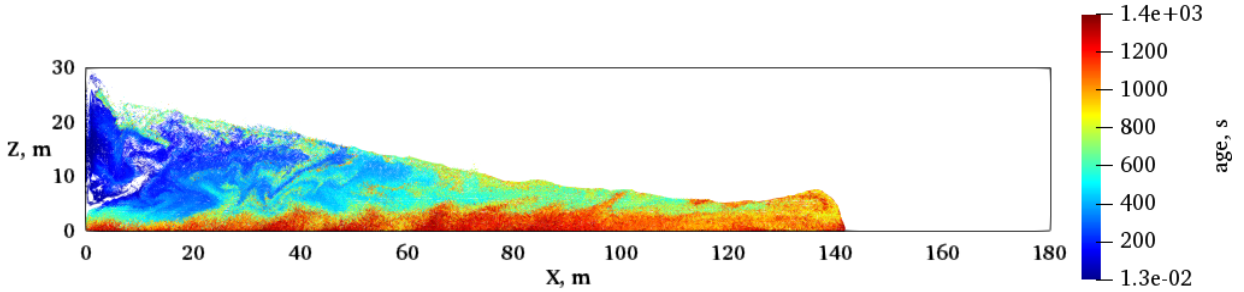

Figure 61. Age Plot of Proppant Distribution at 24 min for Proppant Concentration 2.5 lb/gal

3.6 Case Study 5 – Injection Rate

An investigation was carried out to understand the role of injection rate in proppant placement. Injection time is also normalized to study the sensitivity of injection rate. The pumping rates varied in this case study are 10 bpm and 20 bpm (cases 14 and 15). According to the

comparison between each case at the same injection time and normalized time (**Figures 62-64** and **Figures 71-73**), the proppant length would not increase dramatically with a higher injection rate at normalized injection time. Our results show that the proppant height was increasing faster, with a lower injection rate (**Figures 65, 68, 71**). When the injection was completed, these three cases reach nearly the same proppant height and length (**Figures 71-73**). **Figures 65-73** show the evolution of proppant distribution at 0.3, 0.5, 1.0 of normalized injection time for three different injection rates. This result indicates that increasing the injection rate without adding proppants does not guarantee a significant increase in proppant length.

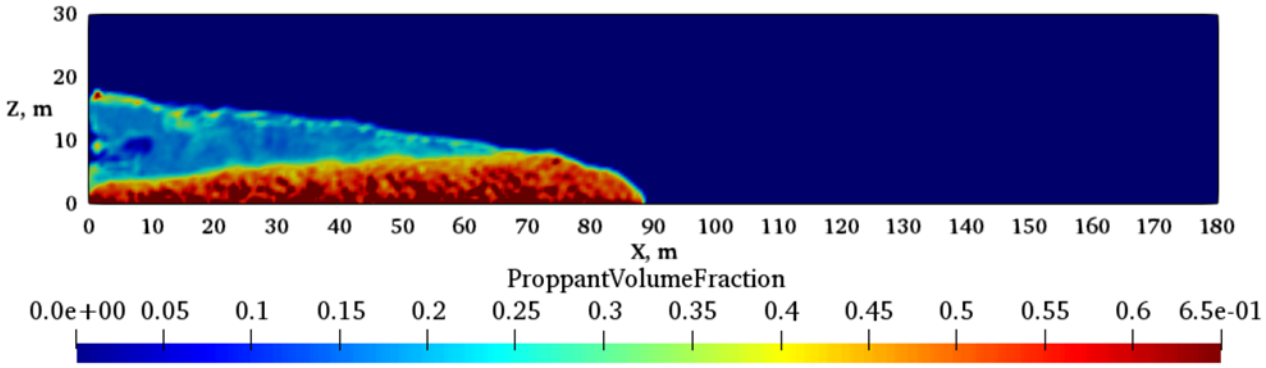

Figure 62. Proppant Volume Fraction Distribution at 21 min for Injection Rate 10 bpm

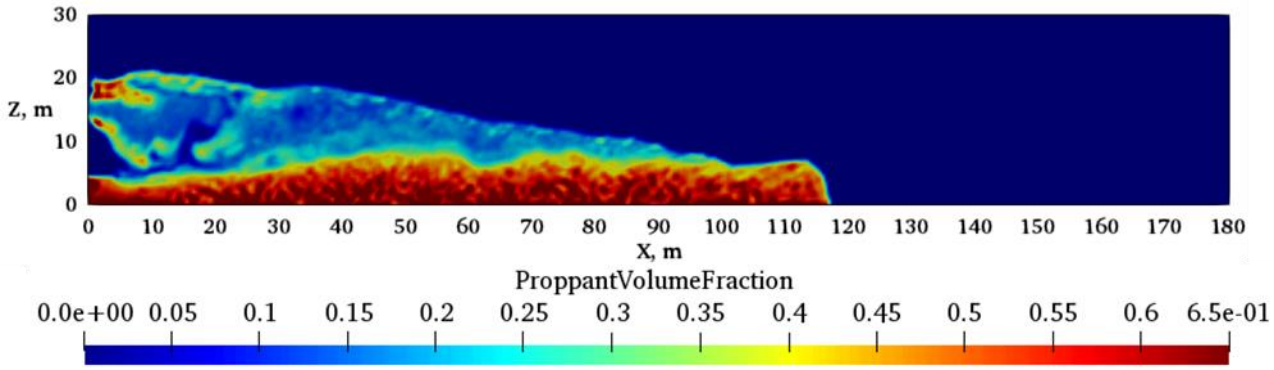

Figure 63. Proppant Volume Fraction Distribution at 21 min for Injection Rate 15 bpm

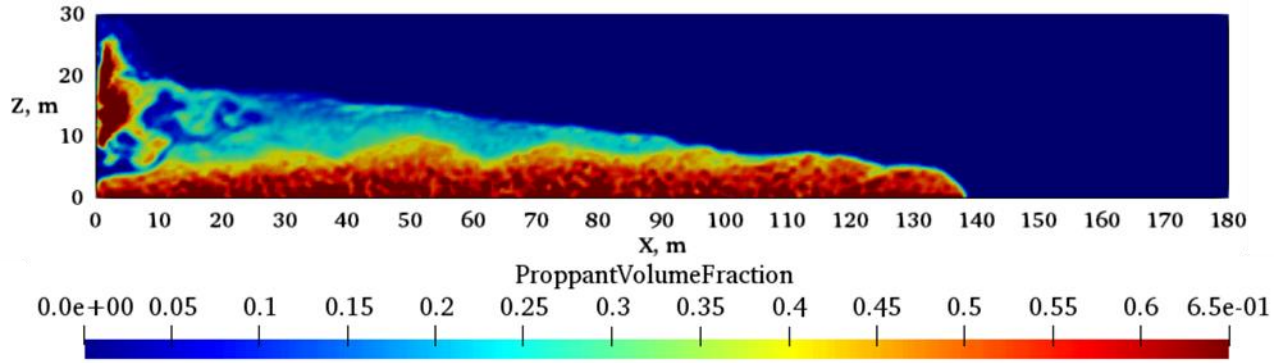

Figure 64. Proppant Volume Fraction Distribution at 21 min for Injection Rate 20 bpm

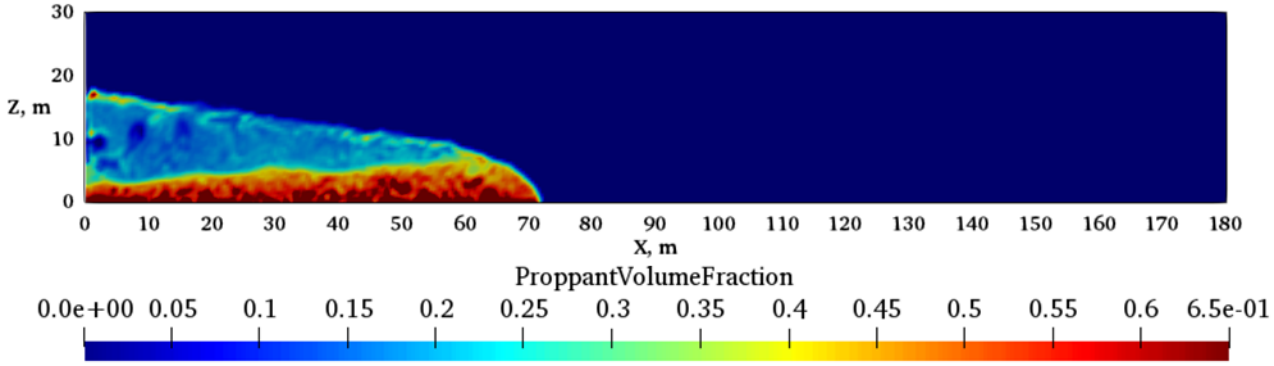

Figure 65. Proppant Volume Fraction Distribution at 15 min for Injection Rate 10 bpm

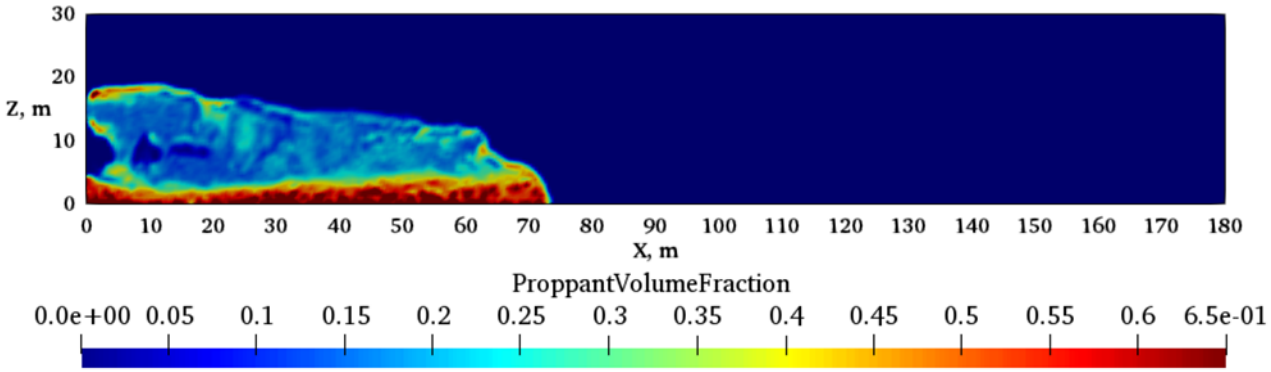

Figure 66. Proppant Volume Fraction Distribution at 10 min for Injection Rate 10 bpm

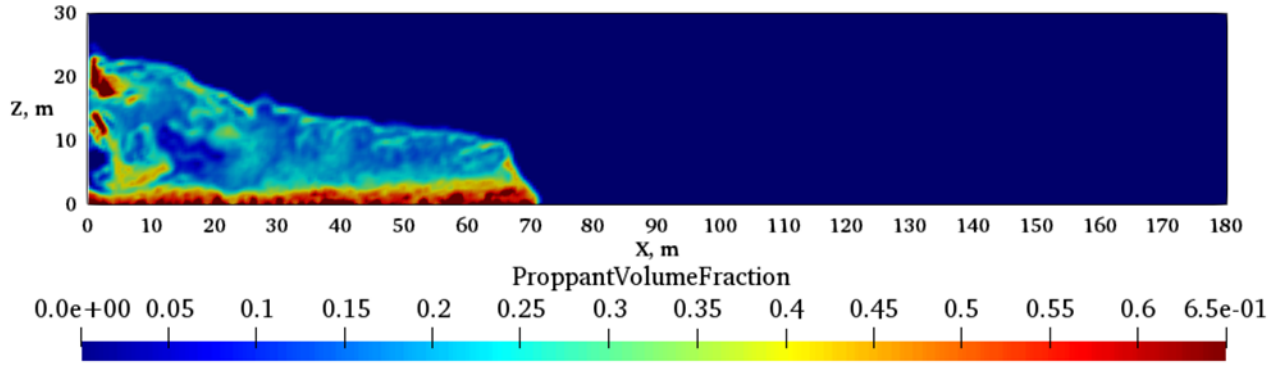

Figure 67. Proppant Volume Fraction Distribution at 7.5 min for Injection Rate 10 bpm

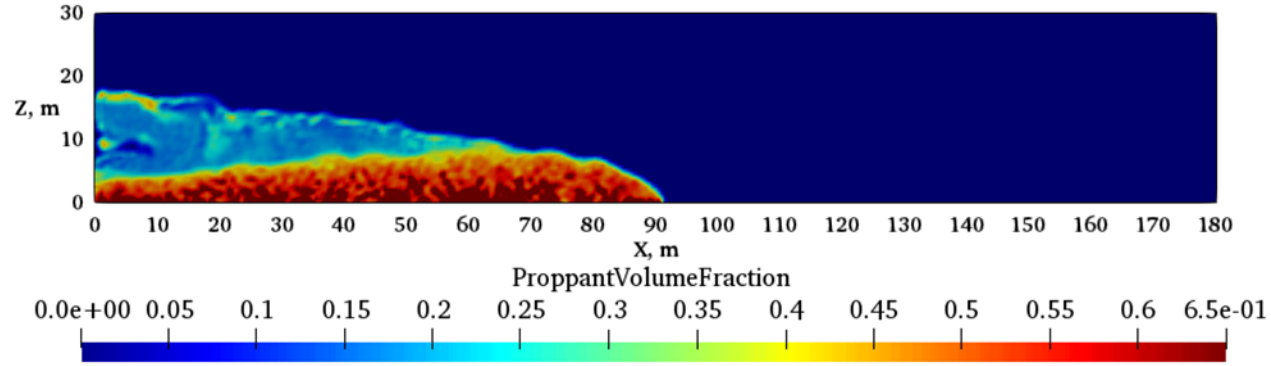

Figure 68. Proppant Volume Fraction Distribution at 22.5 min for Injection Rate 10 bpm, Reprinted from Zhang (2020)

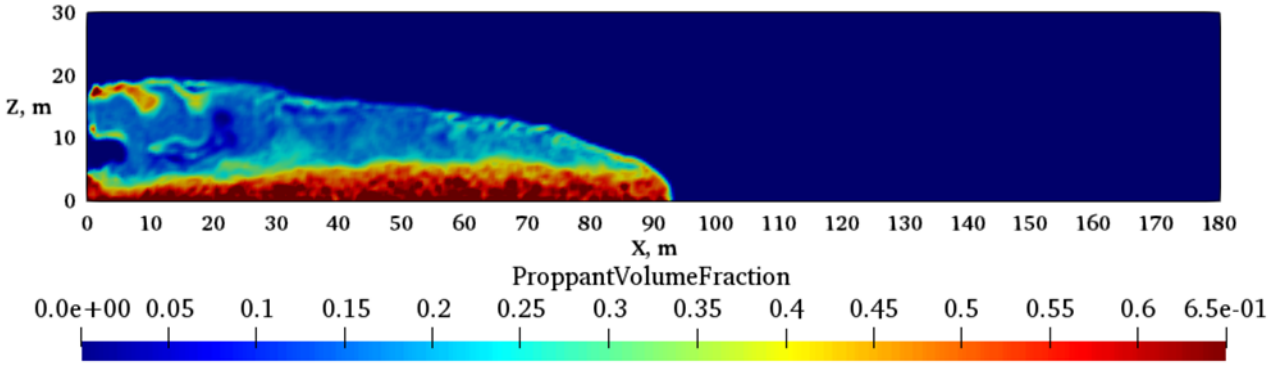

Figure 69. Proppant Volume Fraction Distribution at 15 min for Injection Rate 15 bpm, Reprinted from Zhang (2020)

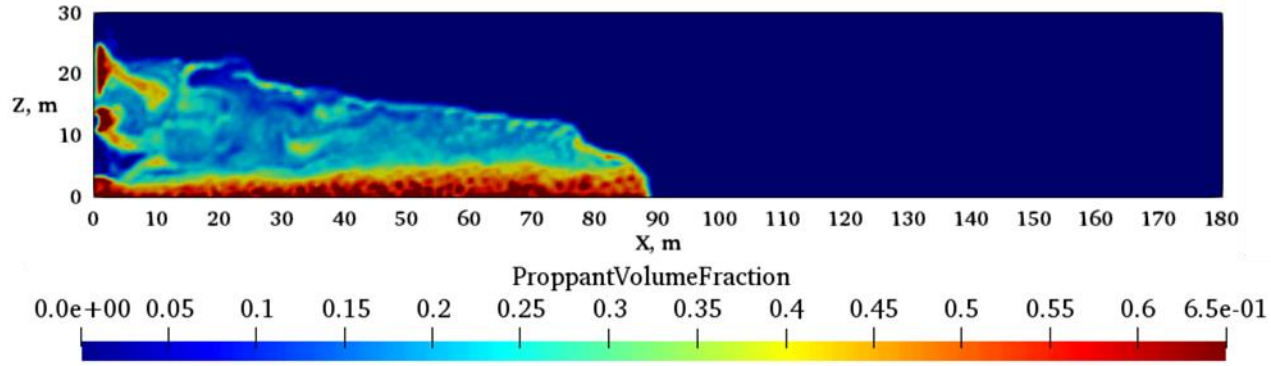

Figure 70. Proppant Volume Fraction Distribution at 11 min for Injection Rate 20 bpm, Reprinted from Zhang (2020)

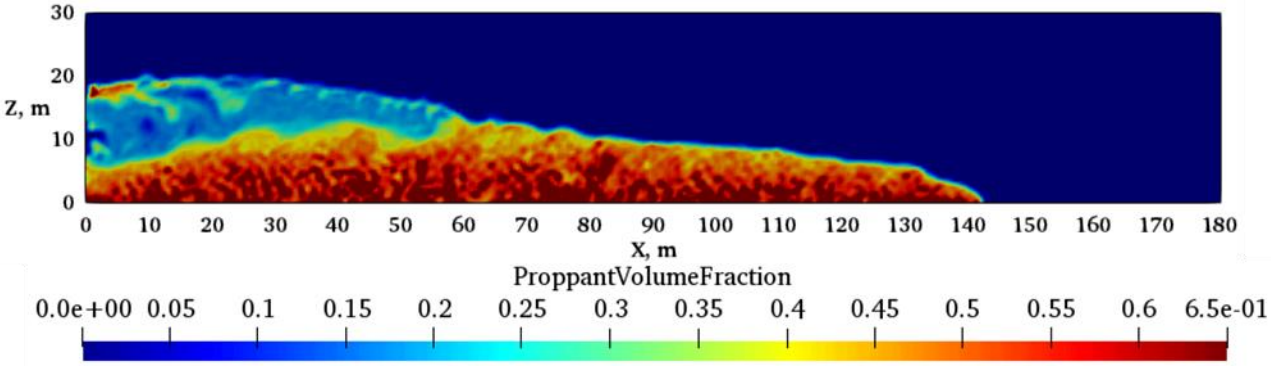

Figure 71. Proppant Volume Fraction Distribution at 45 min for Injection Rate 10 bpm, Reprinted from Zhang (2020)

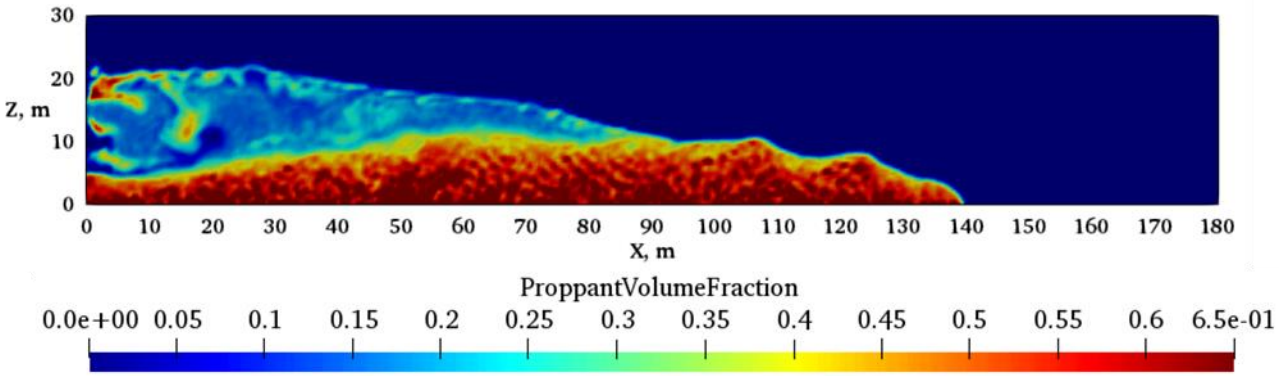

Figure 72. Proppant Volume Fraction Distribution at 30 min for Injection Rate 15 bpm, Reprinted from Zhang (2020)

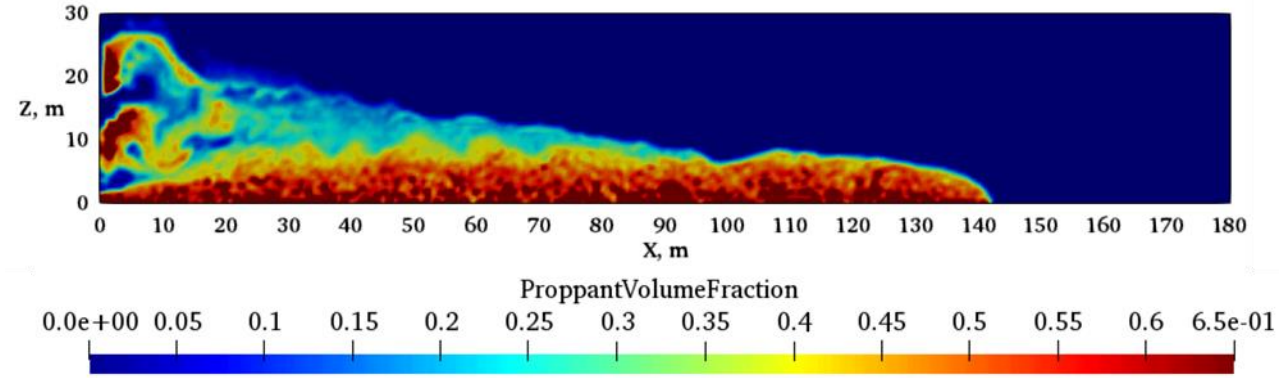

Figure 73. Proppant Volume Fraction Distribution at 22.5 min for Injection Rate 20 bpm, Reprinted from Zhang (2020)

To further investigate the effect of injection rate, we provide the proppant distribution according to their injected time **(Figures 74-76)**. As displayed in the figure, the proppants reached the same length regardless of the injection rate. On the other hand, newly injected proppant and old proppants placed at different locations with different injection rates. The oldest proppants at a lower injection rate could distribute closer to the injection point, and the following proppants injected placed on the other side. The same observation was obtained in the first proppant transport experiment of Kern et al. (1959).

In contrast to the higher injection rate, the oldest proppants with lower injection rates traveled to near the outlet side, while the following proppants placed on the top of previous proppants. This difference of proppant distribution can also explain the same proppant length produced with various injection rates. Proppants with a lower injection rate firstly injected tended to settle near the inlet, and then the following proppants injected for a longer time moved toward the end by bed load transport. For a higher injection rate case, turbulent transport occurred and enabled the earlier injected proppants directly to place further in a short time. The residual proppants injected later would finally settle near the injection point.

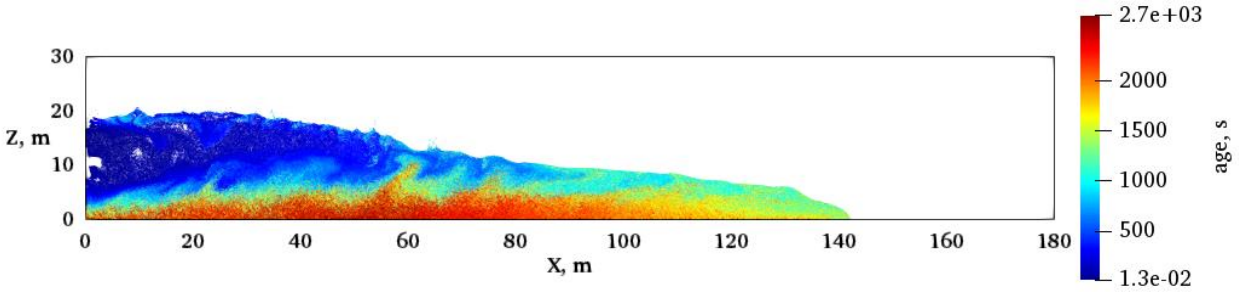

Figure 74. Age Plot of Proppant Distribution at 45 min for Injection Rate 10 bpm, Reprinted from Zhang (2020)

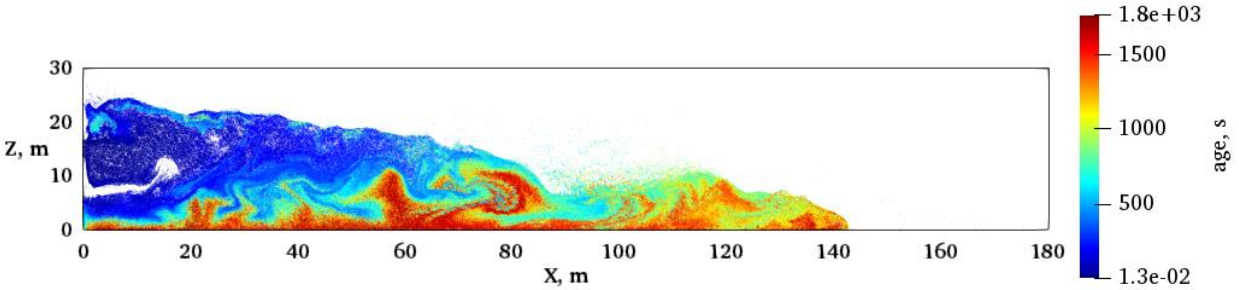

Figure 75. Age Plot of Proppant Distribution at 30 min for Injection Rate 15 bpm, Reprinted from Zhang (2020)

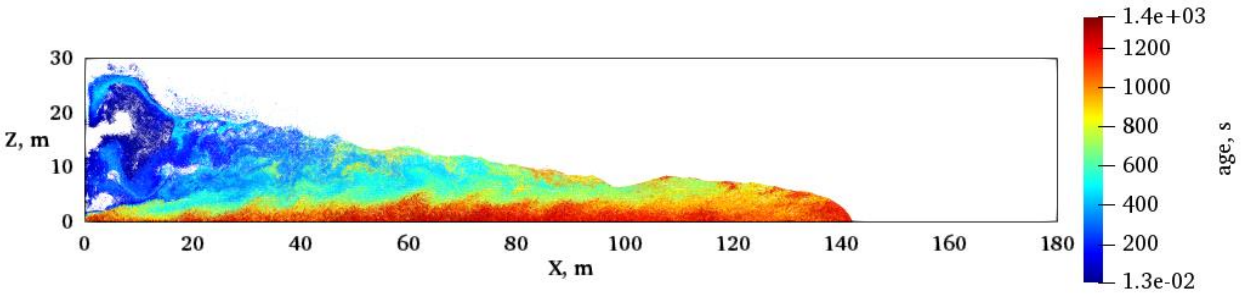

Figure 76. Age Plot of Proppant Distribution at 22.5 min for Injection Rate 20 bpm, Reprinted from Zhang (2020)

4. CONCLUSION[*]

In this research, numerical simulation of proppant transport was studied by using a three-dimensional multiphase particle-in-cell (MP-PIC) method. We validated the model with both CFD-DEM and one reported experimental study, and good agreement was obtained. After that, we conducted a sensitivity analysis and investigated the impact of fracture height, fluid viscosity, proppant concentration, and injection rate on proppant transport.

Although the detailed animation of interactions of particles was captured in results through the MP-PIC model, we still have the following limitations. First, we assumed the geometry of the contact area between wellbore and fracture was rectangular instead of circular. Second, the leak-off effect is not considered in our studies. Third, field-scale fracture geometry was predetermined and static. The effect of dynamic fracture propagation on proppant transport was not considered in this study.

The conclusions can be drawn from this study as follows:

- The multiphase particle-in-cell (MP-PIC) method is a powerful method to address the field scale problem. Also, it can simulate more detailed transport behaviors of particles, such as wash-out effect.

[*] Reprinted with permission from "Numerical Study of Proppant Transport in Field-scale Fractures for Slickwater Fracturing" by Zhang, Z., Mao, S., Shang, Z., Chun, T and Wu, K. 2020. Proceedings of the 54th US Rock Mechanics/Geomechanics Symposium, Copyright [2020] by American Rock Mechanics Association. paper ARMA 20-1170

- When the fracture reaches a certain height, the increasing fracture height has an insignificant impact on proppant transport in the field while decreasing this height can bring a strong wash-out effect and produce a longer proppant bed.
- The fluid viscosity has a strong influence on proppant placement. With increasing fluid viscosity, the proppant bed height decreases dramatically, and proppant length firstly slightly decreases and then increases. The proppant suspension area can also increase remarkably.
- Injecting slurry with low proppant concentration is an efficient way to increase proppant length.
- The injection rate rarely influences proppant placement unless the quantity of proppant varies, while the newly injected proppant and old proppant can place differently for different injection rates.
- Increasing the proppant concentration and injection rate can respectively help proppants reach equilibrium height and maximum fracture length faster.

REFERENCES

Chu, H. et al., 2019a. Transient pressure analysis of a horizontal well with multiple, arbitrarily shaped horizontal fractures. *Journal of Petroleum Science and Engineering*, 180: 631-642. doi: 10.1016/j.petrol.2019.06.003

Chu, H. et al., 2019b. Pressure transient analysis in fractured reservoirs with poorly connected fractures. Journal of Natural Gas Science and Engineering, 67: 30-42. doi: 10.2118/191246-MS

Zhang, R. et al., 2018. Hydraulic fracturing initiation and near-wellbore nonplanar propagation from horizontal perforated boreholes in tight formation. *Journal of Natural Gas Science and Engineering*, 55: 337-349. doi: 10.1016/j.jngse.2018.05.021

Zhang, R. et al., 2020. Hydraulic fracture propagation behavior and diversion characteristic in shale formation by temporary plugging fracturing. *Journal of Petroleum Science and Engineering*, 190. doi: 10.1016/j.petrol.2020.107063

Li, Y., M. Long, L. Zuo, W. Li and W. Zhao, 2019. Brittleness evaluation of coal based on statistical damage and energy evolution theory. *Journal of Petroleum Science and Engineering*, 172: 753-763. doi: 10.1016/j.petrol.2018.08.069

Li, Y., M. Long, J. Tang, M. Chen and X. Fu, 2020. A hydraulic fracture height mathematical model considering the influence of plastic region at fracture tip. *Petroleum Exploration and Development*, 47(1): 184-195. doi: 10.1016/S1876-3804(20)60017-9

Guo, X., K. Wu, J. Killough and J. Tang, 2019. Understanding the Mechanism of Interwell Fracturing Interference With Reservoir/Geomechanics/Fracturing Modeling in Eagle Ford Shale. *SPE-171577-PA*, 22(03): 842-860. doi: 0.15530/URTEC-2018-2874464

Liu, Y., J.Y. Leung, R. Chalaturnyk and C.J.J. Virues, 2017. Fracturing Fluid Distribution in Shale Gas Reservoirs Due to Fracture Closure, Proppant Distribution and Gravity Segregation, *SPE Unconventional Resources Conference*. Society of Petroleum Engineers, Calgary, Alberta, Canada, pp. 21. doi: 10.2118/185043-MS

Liu, Y., J.Y. Leung and R. Chalaturnyk, 2018. Geomechanical Simulation of Partially Propped Fracture Closure and Its Implication for Water Flowback and Gas Production. *SPE-171577-PA*, 21(02): 273-290. doi: 10.2118/189454-PA

Tang, J. et al., 2019. Investigation of Rupture and Slip Mechanisms of Hydraulic Fractures in Multiple-Layered Formations. SPE Journal, 24(05): 2292-2307. doi: doi.org/10.2118/197054-PA

Weng, X., 2015. Modeling of complex hydraulic fractures in naturally fractured formation. Journal of Unconventional Oil and Gas Resources, 9: 114-135. doi: 10.1016/j.juogr.2014.07.001

Wu, R. et al., 2018. Numerical investigation of fluid injection into poorly consolidated geomaterial considering shear dilation and compaction. Journal of Petroleum Science and Engineering, 168: 119-132. doi: 10.1016/j.petrol.2018.05.006

Rui, W. et al., 2017. Numerical Modeling of Hydraulic Fracture Containment of Tight Sandstone Gas Reservoir, 51st U.S. Rock Mechanics/Geomechanics Symposium. American Rock Mechanics Association, San Francisco, California, USA, pp. 9. paper ARMA-2017-0050

Donaldson, E.C., W. Alam and N. Begum, 2014. Hydraulic fracturing explained: Evaluation, implementation, and challenges. Elsevier.

Kern, L., T. Perkins and R. Wyant, 1959. The mechanics of sand movement in fracturing. *Journal of Petroleum Technology*, 11(07): 55-57. doi: 10.2118/1108-G

Schols, R. and W. Visser, 1974. Proppant bank buildup in a vertical fracture without fluid loss, *SPE European Spring Meeting*. Society of Petroleum Engineers. doi: 10.2118/4834-MS

Blot, M. and W. Medlin, 1985. Theory of sand transport in thin fluids, *SPE Annual Technical Conference and Exhibition*. Society of Petroleum Engineers. doi: 10.2118/14468-MS

Medlin, W., J. Sexton and G. Zumwalt, 1985. Sand transport experiments in thin fluids, *SPE Annual Technical Conference and Exhibition*. Society of Petroleum Engineers. doi: 10.2118/14469-MS

Babcock, R., C. Prokop and R. Kehle, 1967. Distribution of propping agent in vertical fractures, Drilling and Production Practice. American Petroleum Institute. document: API-67-207

Clark, P. and N. Guler, 1983. Prop transport in vertical fractures: settling velocity correlations, *SPE/DOE low permeability gas reservoirs symposium*. Society of Petroleum Engineers. doi: 10.2118/11636-MS

Sievert, J.A., H.A. Wahl, P.E. Clark and M.W. Harkin, 1981. Prop Transport In A Large Vertical Model, *SPE/DOE Low Permeability Gas Reservoirs Symposium*. Society of Petroleum Engineers, Denver, Colorado, pp. 7. doi: 10.2118/9865-MS

Shah, S.N. and D.L. Lord, 1990. Hydraulic fracturing slurry transport in horizontal pipes. *SPE Drilling Engineering*, 5(03): 225-232. doi: 10.2118/18994-PA

McMechan, D. and Shah, S., 1991. Static proppant-settling characteristics of non-Newtonian fracturing fluids in a large-scale test model. SPE Production Engineering, 6(03): 305-312. doi:10.2118/19735-PA

Barree, R. and M. Conway, 1994. Experimental and numerical modeling of convective proppant transport, *SPE Annual Technical Conference and Exhibition*. Society of Petroleum Engineers. doi: 10.2118/28564-PA

Clark, P. and Q. Zhu, 1995. Flow Visualization of Flow Into 8 Point-Source Fractures II: The Effect of Fracture Non-Uniformity and Fluid Crosslinking, *SPE Production Operations Symposium*. Society of Petroleum Engineers. doi: 10.2118/29503-MS

Liu, Y. and M.M. Sharma, 2005. Effect of fracture width and fluid rheology on proppant settling and retardation: an experimental study, SPE annual technical conference and exhibition. Society of Petroleum Engineers. doi: 10.2118/96208-MS

Sahai, R., J.L. Miskimins and K.E. Olson, 2014. Laboratory results of proppant transport in complex fracture systems, SPE Hydraulic Fracturing Technology Conference. Society of Petroleum Engineers. doi: 10.2118/168579-MS

Alotaibi, M.A. and J.L. Miskimins, 2015. Slickwater proppant transport in complex fractures: new experimental findings & scalable correlation, SPE Annual Technical Conference and Exhibition. Society of Petroleum Engineers. doi: 10.2118/174828-MS

Ahmad, F.A. and J.L. Miskimins, 2019. An Experimental Investigation of Proppant Transport in High Loading Friction-Reduced Systems Utilizing a Horizontal Wellbore Apparatus, Proceedings of the 7th Unconventional Resources Technology Conference. doi: 10.15530/urtec-2019-414

Mohammed Ba Geri and Abdulmohsin Imqam, M.U.o.S.a.T.M.S., King Saud University, 2019. Investigate Proppant Transport with Varying Perforation Density and its Impact on Proppant Dune Development Inside Hydraulic Fractures. doi: 10.2118/195018-MS

Tong, S. and K.K. Mohanty, 2016. Proppant transport study in fractures with intersections. Fuel, 181: 463-477. doi: 10.1016/j.fuel.2016.04.144

Chun, T., Z. Zhang, S. Mao and K. Wu, 2019a. Experimental Study of Proppant Transport in Complex Fractures with Horizontal Bedding Planes for Slickwater Fracturing, Proceedings of the 7th Unconventional Resources Technology Conference. doi: 10.15530/urtec-2019-547

Mohammed Ba Geri, A.I., and Shari Dunn-Norman, Missouri University of Science and Technology, 2018. Proppant Transport Behavior in Inclined Versus Vertical Hydraulic Fractures: An Experimental Study. doi: 10.2118/191813-18ERM-MS

Chun, T., Y. Li and K. Wu, 2019b. Comprehensive experimental study of proppant transport in an inclined fracture. Journal of Petroleum Science and Engineering. doi: 10.1016/j.petrol.2019.106523

Ariyaratne, W.K.H., E.V.P.J. Manjula, C. Ratnayake and M.C. Melaaen, 2018. CFD Approaches for Modeling Gas-Solids Multiphase Flows - A Review, *Proceedings of The 9th EUROSIM Congress on Modelling and Simulation, EUROSIM 2016, The 57th SIMS Conference on Simulation and Modelling SIMS 2016*, pp. 680-686. doi: 10.3384/ecp17142680

Kong, X., J. McAndrew and P. Cisternas, 2016. CFD study of using foam fracturing fluid for proppant transport in hydraulic fractures, Abu Dhabi International Petroleum Exhibition & Conference. Society of Petroleum Engineers. doi: 10.2118/183549-MS

Clark, P.E., 2006. Transport of proppant in hydraulic fractures, SPE Annual Technical Conference and Exhibition. Society of Petroleum Engineers. doi: 10.2118/103167-MS

Kong, X. and J. McAndrew, 2017. A Computational Fluid Dynamics Study of Proppant Placement in Hydraulic Fracture Networks, SPE Unconventional Resources Conference. Society of Petroleum Engineers, Calgary, Alberta, Canada, pp. 14. doi:10.2118/185083-MS

Zeng, J., H. Li and D. Zhang, 2019. Numerical simulation of proppant transport in propagating fractures with the multi-phase particle-in-cell method. Fuel, 245: 316-335. doi: 10.1016/j.fuel.2019.02.056

Zhang, M., C.-H. Wu and M. Sharma, 2019. Proppant Placement in Perforation Clusters in Deviated Wellbores, *Proceedings of the 7th Unconventional Resources Technology Conference*. doi: 10.15530/urtec-2019-298

Kou, R., G. Moridis and T. Blasingame, 2018a. Analysis and Modeling of Proppant Transport in Inclined Hydraulic Fractures, *SPE Hydraulic Fracturing Technology Conference and Exhibition*. Society of Petroleum Engineers. doi: 10.2118/189856-MS

Kou, R., G.J. Moridis and T. Blasingame, 2018b. Field Scale Proppant Transport Simulation and Its Application to Optimize Stimulation Strategy, *Proceedings of the 6th Unconventional Resources Technology Conference*. doi: 10.15530/URTEC-2018-2878230

Mao, S., Z. Shang, S. Chun, J. Li and K. Wu, 2019. An efficient three-dimensional multiphase particle-in-cell model for proppant transport in the field scale, Unconventional Resources Technology Conference, Denver, Colorado, 22-24 July 2019. Unconventional Resources Technology Conference (URTeC); Society of Petroleum Engineers, pp. 2486-2501. doi: 10.105530/urtec-2019-462

Hu, X. et al., 2018. A new model for simulating particle transport in a low-viscosity fluid for fluid-driven fracturing. *AIChE Journal*, 64(9): 3542-3552. doi: 10.1002/aic.16183

Patel, P.S., C.J. Robart, M. Ruegamer and A. Yang, 2014. Analysis of US Hydraulic Fracturing Fluid System and Proppant Trends, SPE Hydraulic Fracturing Technology Conference. Society of Petroleum Engineers, The Woodlands, Texas, USA, pp. 20. doi: 10.2118/168645-MS

Ba Geri, M., A. Ellafi, R. Flori, J. Noles and S. Kim, 2019. Viscoelastic Characterization Effect of High-Viscosity Friction Reducers and Proppant Transport Performance in High-TDS Environment, SPE Annual Technical Conference and Exhibition. Society of Petroleum Engineers, Calgary, Alberta, Canada, pp. 15. doi:10.2118/196014-MS

Suri, Y., S.Z. Islam and M. Hossain, 2019. A new CFD approach for proppant transport in unconventional hydraulic fractures. Journal of Natural Gas Science and Engineering, 70 doi: 10.1016/j.jngse.2019.102951

Zhang, Z., Mao, S., Shang, Z., Chun, T and Wu, K. 2020. Numerical Study of Proppant Transport in Field-scale Fractures for Slickwater Fracturing, Proceedings of the 54th US Rock Mechanics/Geomechanics Symposium. American Rock Mechanics Association. paper ARMA 20-1170

Andrews, M.J. and P.J. O'Rourke, 1996. The multiphase particle-in-cell (MP-PIC) method for dense particulate flows. *International Journal of Multiphase Flow*, 22(2): 379-402. doi: 10.1016/0301-9322(95)00072-0

Mao, S., Siddhamshetty, P., Zhang, Z., Yu, W., Chun, T and Wu, K. 2020. Impact Of Proppant Pumping Schedule On Well Production For Slickwater Fracturing, Proceedings of the 8th Unconventional Resources Technology Conference. doi: 10.15530/urtec-2020-2630

Wen, C.Y. and Yu, Y.H. (1966) Mechanics of Fluidization. *The Chemical Engineering Progress Symposium Series*, 162, 100-111.

Harris, S. and D. Crighton, 1994. Solitons, solitary waves, and voidage disturbances in gas-fluidized beds. *Journal of Fluid Mechanics*, 266: 243-276. doi: 10.1017/S0022112094000996

Auzerais, F., R. Jackson and W. Russel, 1988. The resolution of shocks and the effects of compressible sediments in transient settling. *Journal of Fluid Mechanics*, 195: 437-462. doi: 10.1017/S0022112088002472

Snider, D.M., 2001. An Incompressible Three-Dimensional Multiphase Particle-in-Cell Model for Dense Particle Flows. *Journal of Computational Physics*, 170(2): 523-549. doi: 10.1006/jcph.2001.6747

Tsai, K., E. Fonseca, E. Lake and S. Degaleesan, 2012. Advanced computational modeling of proppant settling in water fractures for shale gas production. Spe Journal, 18(01): 50-56. doi: 10.2118/151607-MS